INTERNATIONAL JOURNAL OF
NUMERICAL ANALYSIS AND MODELING
Volume 20, Number 6, Pages 772–804

doi: 10.4208/ijnam2023-1034

A POSTERIORI ERROR ESTIMATES FOR A LOCAL DISCONTINUOUS GALERKIN APPROXIMATION OF SEMILINEAR SECOND-ORDER ELLIPTIC PROBLEMS ON CARTESIAN GRIDS

MAHBOUB BACCOUCH

Abstract. In this paper, we design and analyze new residual-type *a posteriori* error estimators for the local discontinuous Galerkin (LDG) method applied to semilinear second-order elliptic problems in two dimensions of the type $-\Delta u = f(\mathbf{x}, u)$. We use our recent superconvergence results derived in *Commun. Appl. Math. Comput. (2021)* to prove that the LDG solution is superconvergent with an order $p+2$ towards the p-degree right Radau interpolating polynomial of the exact solution, when tensor product polynomials of degree at most p are considered as basis for the LDG method. Moreover, we show that the global discretization error can be decomposed into the sum of two errors. The first error can be expressed as a linear combination of two $(p+1)$-degree Radau polynomials in the x- and $y-$ directions. The second error converges to zero with order $p+2$ in the L^2-norm. This new result allows us to construct *a posteriori* error estimators of residual type. We prove that the proposed *a posteriori* error estimators converge to the true errors in the L^2-norm under mesh refinement at the optimal rate. The order of convergence is proved to be $p+2$. We further prove that our *a posteriori* error estimates yield upper and lower bounds for the actual error. Finally, a series of numerical examples are presented to validate the theoretical results and numerically demonstrate the convergence of the proposed *a posteriori* error estimators.

Key words. local discontinuous Galerkin method, semilinear elliptic problems, *a posteriori* error estimators, superconvergence, Radau polynomial.

1. Introduction

The *a posteriori* error estimates are computable quantities from numerical solutions. They can be used for mesh modification such as refinement or coarsening [50]. In this work, we design and analyze *a posteriori* error estimators for the local discontinuous Galerkin (LDG) for the following semilinear second-order elliptic problems of the form

$$-\Delta u = f(\mathbf{x}, u), \quad \mathbf{x} \in \Omega. \tag{1a}$$

In our analysis we assume that the nonlinear function $f : \overline{\Omega} \times \mathbb{R} \to \mathbb{R}$ is smooth with respect to its arguments. Since *a priori* error estimates provided in [25] will be used, we make the same assumption on f. To be more precise, we always assume that f and its partial derivatives are continuous for $\mathbf{x} \in \overline{\Omega}$ and $u \in \mathbb{R}$ and satisfies the following uniform bound

$$|f(\mathbf{x}, u)| \leq M, \quad \forall\, \mathbf{x} \in \Omega, \quad \forall\, u \in \mathbb{R}, \tag{1b}$$

as well as the Lipschitz condition

$$|f_u(\mathbf{x}, u) - f_u(\mathbf{y}, v)| \leq L\left(\|\mathbf{x} - \mathbf{y}\| + |u - v|\right), \quad \forall\, \mathbf{x},\ \mathbf{y} \in \Omega, \quad \forall\, u,\ v \in \mathbb{R}. \tag{1c}$$

We focus on two dimensions and write $\mathbf{x}$ as (x, y). Without loss of generality, we consider a rectangular domain denoted by $\Omega = \{\mathbf{x} = (x, y) :\ a < x < b,\ c < y < d\}$.

Received by the editors on June 19, 2022 and, accepted on July 4, 2023.
2000 *Mathematics Subject Classification.* 65N12, 65N15, 65N30, 65N50.

Here, we remark that our results remain true, with minor changes in the proofs, when Ω is a rectangular bounded domain of $\mathbb{R}^3$. In this paper, we will consider either periodic boundary conditions

$$\begin{aligned} &u(a,y) = u(b,y),\ u(x,c) = u(x,d), \\ &u_x(a,y) = u_x(b,y), \quad u_y(x,c) = u_y(x,d),\ (x,y) \in \partial\Omega, \end{aligned} \tag{1d}$$

or purely Dirichlet boundary conditions

$$u = g_D, \quad (x,y) \in \partial\Omega, \tag{1e}$$

or mixed Dirichlet-Neumann boundary conditions

$$u = g_D, \quad (x,y) \in \partial\Omega_D, \quad \mathbf{n} \cdot \nabla u = \mathbf{n} \cdot \mathbf{g}_N, \quad (x,y) \in \partial\Omega_N. \tag{1f}$$

Here, $\mathbf{n}$ is the outward unit normal to the boundary, $\partial\Omega$, of Ω. For the mixed boundary conditions (1f), we make the assumption that the boundary $\partial\Omega = \partial\Omega_D \cup \partial\Omega_N$ is decomposed into two disjoint sets denoted by $\partial\Omega_D$ and $\partial\Omega_N$, where Dirichlet and Neumann boundary conditions are imposed, respectively. In addition, we assume that the measure of the Dirichlet boundary $\partial\Omega_D$ is nonzero. In our analysis, we assume that the given functions f, g_D, and $\mathbf{g}_N$ are smooth functions on their domains such that the problem (1) has one and only one solution $u \in H^2(\Omega)$. We refer the reader to [37, 39, 41] and the references therein for the existence and uniqueness of solutions to general elliptic problems.

Among the numerous numerical schemes used to solve elliptic problems, the discontinuous Galerkin (DG) finite element methods constitute an important class. In recent years, DG methods have been proven to be powerful and popular computational methods for the numerical solution of partial differential equations. They have been successfully applied to approximate solutions to many linear and nonlinear time-independent as well as time-dependent problems. The DG method was originally proposed by Reed and Hill in [46] to solve hyperbolic conservation laws with only first-order spatial derivatives. A major development of the DG method is the so-called Runge-Kutta DG (RKDG) framework proposed for solving nonlinear hyperbolic conservation laws containing first order spatial derivatives in a series of papers by Cockburn, Shu *et al.*. Later, serval DG methods were designed to deal with equations involving higher order derivatives. The DG method has many attractive features compared with the classical numerical methods such as finite difference and finite element methods. The main advantages of these DG methods include the high order accuracy, geometric flexibility, suitability for $h-$ and $p-$adaptivity, extremely local data structure, high parallel efficiency and a good theoretical foundation for stability and error estimates. We refer the reader to [33, 45, 47, 48] for more information on many DG methods and their applications.

The DG method was later generalized to the so-called local discontinuous Galerkin (LDG) method by Cockburn and Shu to solve problems with higher order spatial derivatives, such as convection-diffusion equations [35, 51], wave equations [10, 13], and other third- and fourth-order problems [36, 44, 53]. The LDG method shares all the nice features of the DG methods for hyperbolic equations, and it becomes one of the most popular numerical methods for solving elliptic problems. The main idea of the LDG method is to convert the original differential equation into a system of first-order differential equations by introducing some auxiliary variables, and then discretize the resulting system with the classical DG method for first-order equations. With carefully chosen numerical fluxes, the stability and convergence of the LDG methods have been studied for many linear and nonlinear model problems. After that, the LDG method has been a popular way to solve many problems with

higher order spatial derivatives, including second- and fourth-order boundary-value problems for ordinary differential equations (ODEs) [22, 24], convection-diffusion equations [1, 11, 20], second-order wave equations [10, 13], sine-Gordon equations [18, 23], third-order KdV type equations [21] and fourth-order problems [12, 36], and many other linear and nonlinear equations.

Arnold *et al.* [8] proved that approximations of the potential and the flux, given by consistent and stable DG methods, converge in the L^2-norm with order $p+1$ and p, respectively, for any $p \geq 1$, when piecewise polynomials of degree $p \geq 1$ are used as approximating spaces. In [31], the authors have discussed stability and order of convergence of the LDG method applied to the Laplace equation. With a specific choice of numerical fluxes, it is shown in [31] that the discrete potential u_h and its flux $\mathbf{q}_h$, where u_h and $\mathbf{q}_h$ are, respectively, the LDG approximations to u and $\mathbf{q} = \nabla u$, converge in L^2-norm with order $p+1$ and p, respectively, for any $p \geq 1$. Subsequently, the authors in [40] have discussed the LDG method for quasilinear elliptic boundary-value problems and they have shown that u_h and $\mathbf{q}_h$ converge in L^2-norm with order $p+1$ and p, respectively. In [34], Cockburn *et al.*, presented a superconvergence result for the LDG method for the linear elliptic problem on Cartesian grids. They identified a special numerical flux for which the L^2-norm of the gradient and the L^2-norm of the potential are of orders $p+1/2$ and $p+1$, respectively, when tensor product polynomials of degree at most p are used. In [9], Cockburn and Dong analyzed the so-called the minimal dissipation local discontinuous Galerkin method (md-LDG) for convection-diffusion or diffusion problems. The distinctive feature of this method is that the stabilization parameters associated with the numerical trace of the flux are identically equal to zero in the interior of the domain; this is why its dissipation is said to be minimal. They showed that the orders of convergence of the approximations for the potential and the flux using polynomials of degree p are the same as those of all known discontinuous Galerkin methods, namely, $(p+1)$ and p, respectively. Their numerical results suggest that these orders of convergence are sharp. The novelty of the analysis is that it bypasses a seemingly indispensable condition, namely, the positivity of the above mentioned stabilization parameters, by using a new, carefully defined projection tailored to the very definition of the numerical traces. More recently, Adjerid and Chaabane [2] improved the results in [34]. They proved that, by approximating Dirichlet boundary conditions with appropriate projections or interpolations, both the LDG solution and its gradient on Cartesian meshes are of order $p+1$ in the L^2-norm. More specifically, they improved the estimate for the solution gradient by a factor $\sqrt{h}$.

A posteriori error estimates can be used to evaluate the solution errors of the discrete problem without requiring any *a priori* information on the exact solution. Indeed, the *a posteriori* analysis controls the overall discretization error of a problem by providing error indicators that are easy to compute. Once these error indicators are constructed, their efficiency can be proven by bounding each indicator by the local error. *A posteriori* error estimations have been studied for several types of partial differential equations. We refer the reader to [7, 28, 38, 50] and the references therein.

A posteriori error estimates provide very useful indications of the accuracy of the approximations as they tell us how well a given approximation is without knowing the exact solution. They further provide the basis of adaptive mesh refinement (AMR). An AMR algorithm refines grids by placing finer and finer subgrids in the different portions of the computational domain where they are required. The

typical AMR algorithm for elliptic problems is based on the following procedure *solve* $\rightarrow$ *estimate* $\rightarrow$ *mark* $\rightarrow$ *refine*. In the first step we solve the problem on an initial mesh. In the second step, we estimate the error using the *a posteriori* error bound which is the purpose for this paper. In the third step, we mark a subset of elements for refinement. In the last step, we refine the elements marked for refinement. The process can be repeated until the solution is sufficiently accurate.

A wide variety of *a posteriori* error estimators are available for second-order elliptic problems. Karakashian and Pascal [43] proposed *a posteriori* error estimates for a DG approximation of second-order elliptic problem on triangular partition. Bustinza *et al.* [29] presented a residual-based reliable *a posteriori* error estimator for the LDG approximations of linear and nonlinear diffusion problems. Castillo [30] constructed an *a posteriori* global error estimate for the LDG method for linear second order elliptic problems. Ainsworth *et al.* proposed and studied several *a posteriori* error estimate techniques for DG methods on triangular meshes in a series of papers [3, 4, 5, 6]. In [49], the authors presented a numerical study of an adaptive technique for solving steady fluid flow problems through porous media in 2D using a LDG method. Their technique starts with an initial conformal spatial discretization of the domain and, in each step, the error of the solution is estimated. The mesh is locally modified according to the error estimate by performing two local operations: refinement and agglomeration. This procedure is repeated until the solution reaches a desired accuracy. In [13, 14, 16, 17, 26, 27], Adjerid and Baccouch designed and analyzed several residual-based and recovery-based *a posteriori* DG and LDG error estimates for two-dimensional hyperbolic and elliptic problems on triangular and rectangular meshes.

More recently, we investigated the convergence and superconvergence properties of the LDG method for semilinear second-order elliptic problem in two dimensions (1) using rectangular meshes in [25]. We introduced special Gauss-Radau projections to obtain, under some suitable choice of numerical fluxes, the optimal convergence order in L^2-norm of $\mathcal{O}(h^{p+1})$ for the LDG solution u and its gradient $\mathbf{q} = \nabla u$, when tensor product polynomials of degree at p and grid size h are employed. We further proved that the LDG solutions u_h and $\mathbf{q}_h$ are superconvergent with order $p+2$ toward special Gauss-Radau projections of the exact solutions. These results play a central role in the design and analysis of the proposed *a posteriori* error estimators.

In this paper, we continue the investigation of the LDG method proposed in [25]. The main purpose of this part is to design and analyze efficient residual-based *a posteriori* error estimates for the LDG method for the same model problem (1). We first prove that the error between the LDG solution u_h and the interpolating polynomial that interpolates u at the roots of the $(p+1)$-degree right Radau polynomial achieves $(p+2)$-th order superconvergence in the L^2-norm. This new result allows us to prove that the actual error $u - u_h$ can be decomposed into the sum of two errors. The first error is the significant one and can be expressed as a linear combination of two $(p+1)$-degree Radau polynomials in the x- and $y-$ directions. The second error is less significant and it is shown to converge to zero with order $p+2$ in the L^2-norm. This decomposition allows us to construct *a posteriori* error estimators of residual-type. The *a posteriori* error estimates are shown to converge to the true errors in the L^2-norm under mesh refinement. The order of convergence is proved to be $p+2$. Finally, we show that the proposed estimators are asymptotically exact. Our numerical experiments are in very good agreement with the theoretical orders of convergence. To the best of our knowledge, these results are

novel in the literature. We would like to point out that the present LDG method has several features over the standard numerical methods due to the following nice properties: (i) the LDG method can be easily designed for any order of accuracy (the order of accuracy can be locally determined in each cell, thus allowing for efficient p adaptivity), (ii) it can be used on arbitrary triangulations, even those with hanging nodes, thus allowing for efficient h-adaptivity, (iii) the LDG method provides optimal convergence properties for both the solution and the auxiliary variables that approximate its derivatives, (iv) the LDG method is extremely local in data communications (the evolution of the solution in each cell needs to communicate only with the immediate neighbors, regardless of the order of accuracy, thus allowing for efficient parallel implementations), and (iv) it achieves superconvergence properties, which play a key role to construct asymptotically exact *a posteriori* error estimators.

The remainder of this paper is organized as follows. In Section 2, we recall the LDG scheme for the second-order elliptic BVP (1). We also present some preliminary results which will be used throughout this paper. Sections 3 and 4 are the main sections of the present paper, where superconvergence error analysis and *a posteriori* error estimation are discussed in details. Extensive numerical experiments are given in Section 5 to illustrate the theoretical convergence rates proved in Sections 3 and 4. Finally, in Section 6, we conclude with a short discussion of possible extensions and a description of our forthcoming work.

2. The LDG method and Preliminaries

This section is devoted to the definition of the LDG method. We also provide some notation, projections, and the *a priori* error estimates provided in [25].

2.1. The LDG scheme. Here, we define the finite element spaces and proceed to construct the LDG scheme. First, let us introduce a new auxiliary variable $\mathbf{q} = \nabla u$ and write the model problem in the following mixed form [25]

$$-\nabla \cdot \mathbf{q} = f(x, y, u), \tag{2a}$$

$$\mathbf{q} - \nabla u = \mathbf{0}. \tag{2b}$$

Let $\mathcal{T}_h$ be Cartesian mesh of the domain $\overline{\Omega} = [a, b] \times [c, d]$. We assume that the mesh consists of $N = n \times m$ rectangular elements $K = I_i \times J_j$, where $I_i = [x_{i-1}, x_i],\ i = 1, 2, \ldots, n$ and $J_j = [y_{j-1}, y_j],\ j = 1, 2, \ldots, m$ where

$$a = x_0 < x_1 < \cdots < x_n = b, \quad c = y_0 < y_1 < \cdots < y_m = d.$$

For each rectangle $K \in \mathcal{T}_h$, we denote the mesh sizes as $h_i = x_i - x_{i-1}$ and $k_j = y_j - y_{j-1}$. The maximal mesh size is denoted by $h = \max_{1 \le i \le n,\ 1 \le j \le m} (h_i, k_j)$. In this paper, we assume the mesh $\mathcal{T}_h$ is a shape regular triangulation of Ω, characterized by a small parameter h, namely that there exists a constant $c_0 > 0$ such that $c_K \ge c_0,\ \forall\ K \in \mathcal{T}_h$. Here c_K is the so-called chunkiness parameter defined by $c_K = h_K / d_K$, where $h_K = \max(h_i, k_j)$ is the local mesh size defined as the length of the longest edge of the element K and d_K is the diameter of the inscribed circle.

The LDG weak formulation is obtained by multiplying the two equations in (2) by sufficiently smooth test functions v and $\mathbf{w}$, respectively, integrating over an

arbitrary rectangle $K \in \mathcal{T}_h$, and applying Green's Theorem

$$\iint_K \mathbf{q} \cdot \nabla v \; dxdy - \int_\Gamma \mathbf{n} \cdot \mathbf{q} \; vds = \iint_K f(x,y,u) \; v \; dxdy, \tag{3a}$$

$$\iint_K \mathbf{q} \cdot \mathbf{w} \; dxdy + \iint_K u \; \nabla \cdot \mathbf{w} \; dxdy - \int_\Gamma u \; \mathbf{n} \cdot \mathbf{w} \; ds = 0, \tag{3b}$$

where $\mathbf{n}$ is the outward normal unit vector to Γ and $\Gamma = \partial K$ is used to denote the boundary of rectangle $K \in \mathcal{T}_h$.

Let $\mathbb{P}^p(I_i)$ and $\mathbb{P}^p(J_j)$ be the spaces of polynomials of degree at most p on the intervals I_i and J_j, respectively. We define the piecewise polynomial finite element space V_h^p as the space of tensor product of $\mathbb{P}^p(I_i)$ and $\mathbb{P}^p(J_j)$, that is

$$V_h^p = \{v \in L^2(\Omega) : \; \Omega \to \mathbb{R} | \;\; v|_K \in \mathcal{Q}^p(K), \; \forall \; K \in \mathcal{T}_h\},$$

where $\mathcal{Q}^p(K)$ is the tensor product space of $\mathbb{P}^p(I_i)$ and $\mathbb{P}^p(J_j)$. We also extend this definition to vector-valued functions as

$$\mathbf{V}_h^p = \{\mathbf{w} \in (L^2(\Omega))^2 : \; \Omega \to \mathbb{R}^2 | \; \mathbf{w}|_K \in (\mathcal{Q}^p(K))^2 , \; \forall \; K \in \mathcal{T}_h\}.$$

The discrete LDG method is now formulated as follows: find $u_h \in V_h^p$ and $\mathbf{q}_h = [q_{1,h}, q_{2,h}]^t \in \mathbf{V}_h^p$ such that

$$\iint_K \mathbf{q}_h \cdot \nabla v \; dxdy - \int_\Gamma \mathbf{n} \cdot \hat{\mathbf{q}}_h \; vds = \iint_K v \; f(x,y,u_h) \; dxdy, \quad \forall \; v \in V_h^p, \tag{4a}$$

$$\iint_K \mathbf{q}_h \cdot \mathbf{w} \; dxdy + \iint_K u_h \; \nabla \cdot \mathbf{w} \; dxdy - \int_\Gamma \hat{u}_h \; \mathbf{n} \cdot \mathbf{w} \; ds = 0, \quad \forall \; \mathbf{w} \in \mathbf{V}_h^p, \tag{4b}$$

for all $K \in \mathcal{T}_h$. The "hat" quantities $\hat{u}_h$ and $\hat{\mathbf{q}}_h$ are the so-called numerical fluxes. They take either the value from one side of the interface (namely inside or outside of the element K) or some linear combination of the values from both sides of the interface. The numerical fluxes need to be designed suitably to ensure consistency, stability, and convergence.

To define the numerical fluxes $\hat{u}_h$ and $\hat{\mathbf{q}}_h$ on the boundary Γ, we introduce some definitions and notation. For $y \in J_j$, we let $v^+(x_i, y)$ and $v^-(x_i, y)$ be the values of the function v at the point (x_i, y) from the right element $I_{i+1} \times J_j$ and from the left element $I_i \times J_j$, respectively. Similarly, for $x \in I_i$, we use $v^+(x, y_j)$ and $v^-(x, y_j)$ to denote the values of v at the point (x, y_j) from the top element $I_i \times J_{j+1}$ and from the bottom element $I_i \times J_j$, respectively, *i.e.*, for $i = 0, 1, \ldots, n$ and $j = 0, 1, \ldots, m$

$$v^\pm(x_i, y) = \lim_{s \to 0^\pm} v(x_i + s, y), \quad y \in J_j, \quad v^\pm(x, y_j) = \lim_{s \to 0^\pm} v(x, y_j + s), \quad x \in I_i.$$

Let K^+ and K^- be two adjacent rectangular elements of the mesh $\mathcal{T}_h$. We consider an arbitrary point (x, y) of the edge $\Gamma = K^+ \cap K^-$ sharing the adjacent elements K^+ and K^-. Let us use $\mathbf{n}^\pm$ to denote the corresponding outward unit normal vectors at that point. Let $(v^\pm, \mathbf{w}^\pm)$ be the traces of $(v, \mathbf{w})$ on Γ from the interior of the element $K^\pm$. The mean values $\{\cdot\}$ and jumps $[\![\cdot]\!]$ of a scalar-valued function $v \in V_h^p$ and a vector-valued function $\mathbf{w} \in \mathbf{V}_h^p$ at the point $(x, y) \in \Gamma$ are defined as

$$\{v\} = \frac{1}{2}(v^+ + v^-), \quad \{\mathbf{w}\} = \frac{1}{2}(\mathbf{w}^+ + \mathbf{w}^-),$$
$$[\![v]\!] = v^+\mathbf{n}^+ + v^-\mathbf{n}^-, \quad [\![\mathbf{w}]\!] = \mathbf{n}^+ \cdot \mathbf{w}^+ + \mathbf{n}^- \cdot \mathbf{w}^-.$$

Now, we are in the position to introduce the numerical fluxes [9, 25, 31, 34].

- Numerical fluxes associated with the periodic boundary conditions (1d): We use the following alternating fluxes

$$\hat{u}_h = u_h^- \quad \text{and} \quad \hat{\mathbf{q}}_h = \mathbf{q}_h^+. \tag{4c}$$

We remark that this choice is not particularly restrictive. For example, the other choice $\hat{u}_h = u_h^+$ and $\hat{\mathbf{q}}_h = \mathbf{q}_h^-$ can be used.

- Numerical fluxes associated with the mixed boundary conditions (1f): If Γ is an interior edge then we take

$$\hat{u}_h = \{u_h\} + \mathbf{C}_{12} \cdot [\![u_h]\!] \quad \text{and} \quad \hat{\mathbf{q}}_h = \{\mathbf{q}_h\} - C_{11}[\![u_h]\!] - \mathbf{C}_{12}[\![\mathbf{q}_h]\!], \tag{4d}$$

where $C_{11} \geq 0$ is a stabilization parameter and $\mathbf{C}_{12}$ is a parameter defined on the edge Γ as

$$\mathbf{C}_{12} \cdot \mathbf{n} = \frac{1}{2}\text{sign}(\mathbf{v} \cdot \mathbf{n}).$$

Here, $\mathbf{v}$ is a fixed vector that is not parallel to any normals of element interfaces. It is used to define artificial inflow and outflow boundaries of the domain Ω. The vector $\mathbf{v}$ is employed to provide a single rule for selecting the numerical fluxes $\hat{u}_h$ and $\hat{\mathbf{q}}_h$. For simplicity, we choose $\mathbf{v} = [1, 1]^t$. Then, we define the following artificial inflow boundary $\partial\Omega^-$ and the artificial outflow boundary $\partial\Omega^+$ as

$$\partial\Omega^- = \{(x, y) \in \partial\Omega \mid \mathbf{n} \cdot \mathbf{v} \leq 0\} = \partial\Omega_1^- \cup \partial\Omega_2^-,$$
$$\partial\Omega^+ = \{(x, y) \in \partial\Omega \mid \mathbf{n} \cdot \mathbf{v} > 0\} = \partial\Omega_1^+ \cup \partial\Omega_2^+,$$

where $\partial\Omega_1^-$, $\partial\Omega_2^-$, $\partial\Omega_1^+$, and $\partial\Omega_2^+$ are, respectively, the left, bottom, right, and top edges of the physical domain Ω. We also define the inflow boundary Γ^- and the outflow boundary Γ^+ of each rectangle element $K \in \mathcal{T}_h$ as

$$\Gamma^- = \{(x, y) \in \Gamma \mid \mathbf{n} \cdot \mathbf{v} \leq 0\} = \Gamma_1^- \cup \Gamma_2^-,$$
$$\Gamma^+ = \{(x, y) \in \Gamma \mid \mathbf{n} \cdot \mathbf{v} > 0\} = \Gamma_1^+ \cup \Gamma_2^+,$$

where Γ_1^-, Γ_2^-, Γ_1^+, and Γ_2^+ are, respectively, used to denote the left, bottom, right, and top edges of the rectangle K.

Now, we are ready to define the numerical fluxes if the edge Γ lies on $\partial\Omega$. Using the above definitions, we choose

$$\hat{u}_h = \begin{cases} P_h^- g_D, \ (x, y) \in \partial\Omega_D, \\ u_h^-, \ (x, y) \in \partial\Omega_N \cap \partial\Omega^+, \\ u_h^+, \ (x, y) \in \partial\Omega_N \cap \partial\Omega^-, \end{cases} \tag{4e}$$

$$\hat{\mathbf{q}}_h = \begin{cases} \mathbf{P}_h^+ \mathbf{g}_N, \ (x, y) \in \partial\Omega_N, \\ \mathbf{q}_h^+, \ (x, y) \in \partial\Omega_D \cap \partial\Omega^-, \\ \mathbf{q}_h^+ - C_{11}(u_h^- - P_h^- g_D)\ \mathbf{n}, \ (x, y) \in \partial\Omega_D \cap \partial\Omega^+, \end{cases} \tag{4f}$$

where P_h^- and $\mathbf{P}_h^+$ are special Gauss-Radau projections which will be defined later.

- Numerical fluxes associated with the purely Dirichlet boundary conditions (1e): If the edge Γ lies on $\partial\Omega$ then we take

(4g)

$$\hat{u}_h = P_h^- g_D, \ (x, y) \in \partial\Omega, \quad \hat{\mathbf{q}}_h = \begin{cases} \mathbf{q}_h^+, \ (x, y) \in \partial\Omega \cap \partial\Omega^-, \\ \mathbf{q}_h^+ - C_{11}(u_h^- - P_h^- g_D)\ \mathbf{n}, \ (x, y) \in \partial\Omega \cap \partial\Omega^+. \end{cases}$$

After we define the numerical fluxes $\hat{u}_h$ and $\hat{\mathbf{q}}_h$, the discrete scheme (4) is equivalent to an algebraic system of nonlinear equations for the unknown coefficients appearing

in u_h and $\mathbf{q}_h$. The resulting system can be solved using Newton's method for nonlinear system of equations.

Remark 2.1. *We remark that the LDG method works for general parameters* C_{11} *and* $\mathbf{C}_{12}$*. However, in the remainder of the paper, we present* a priori *and* a posteriori *error analysis for the minimal dissipation LDG (md-LDG) method where* $C_{11} = \mathcal{O}(1)$ *on all edges in* $\mathcal{E}_D^+$ *and* $C_{11} = 0$ *on all other edges. This particular md-LDG method is studied by many authors including* [1, 9, 13, 19, 23, 27, 34]*. We remark that in the md-LDG method, the stabilization parameters associated with the numerical trace of the flux are identically equal to zero for all interior edges; this is why its dissipation is said to be minimal. We would like to mention that Cockburn and Dong* [9] *analyzed the md-LDG for linear convection-diffusion or linear diffusion problems. They showed that the orders of convergence of the approximations for the potential and the flux using polynomials of degree* p *are the same as those of all known discontinuous Galerkin methods, namely,* $(p+1)$ *and* p*, respectively.*

Throughout the paper, we use the following notation:

- Γ_h: the set of all element interfaces of the triangulation $\mathcal{T}_h$,
- Γ_B: the set of all boundary edges of the partition $\mathcal{T}_h$ on $\partial\Omega$,
- $\Gamma_0 = \Gamma_h \backslash \Gamma_B$: the set of all interior interfaces of $\mathcal{T}_h$,
- Γ_B^-: the set of edges on the inflow boundary $\partial\Omega^-$,
- Γ_B^+: the set of edges on the outflow boundary $\partial\Omega^+$,
- $\Gamma_D^\pm = \partial\Omega_D \cap \partial\Omega^\pm$,
- Γ_D, Γ_N, and $\Gamma_D^\pm$, denote the sets of all edges in $\partial\Omega_D$, $\partial\Omega_N$, and $\partial\Omega_D^\pm$, respectively.

2.2. Norms. In this subsection, we define several norms that will be used throughout the paper. Denote $\|u\|_{0,K} = \left(\iint_K u^2(x,y)dxdy\right)^{1/2}$ to be the standard L^2-norm of u on the rectangle $K \in \mathcal{T}_h$. For any natural number ℓ and for $K \in \mathcal{T}_h$, the H^ℓ-norm of a real-valued function $u \in H^\ell(K)$ and $\mathbf{H}^\ell$-norm of a vector-valued function $\mathbf{q} = [q_1, q_2]^t \in \mathbf{H}^\ell(K) = \left(H^\ell(K)\right)^2$ on the rectangle K are defined by

$$\|u\|_{\ell,K} = \left(\sum_{0\le\alpha+\beta\le\ell} \left\| \frac{\partial^{\alpha+\beta}u}{\partial x^\alpha \partial y^\beta} \right\|_{0,K}^2 \right)^{1/2}, \quad \|\mathbf{q}\|_{\ell,K} = \left(\|q_1\|_{\ell,K}^2 + \|q_2\|_{\ell,K}^2\right)^{1/2}.$$

Let Γ_K be the edges of the element K, and we define

$$\|u\|_{\Gamma_K} = \left(\int_{\partial K} u^2(x(s), y(s))ds\right)^{1/2}.$$

We also define the broken Sobolev H^ℓ-norm of u and $\mathbf{H}^\ell$-norm of $\mathbf{q}$ on the whole domain Ω by

$$\|u\|_\ell = \left(\sum_{K\in\mathcal{T}_h} \|u\|_{\ell,K}^2\right)^{1/2}, \quad \|\mathbf{q}\|_\ell = \left(\sum_{K\in\mathcal{T}_h} \|\mathbf{q}\|_{\ell,K}^2\right)^{1/2}.$$

When $\ell = 0$ we drop the subscript from the norm *i.e.*,

$$\|u\| = \left(\sum_{K\in\mathcal{T}_h} \|u\|_{0,K}^2\right)^{1/2}, \quad \|\mathbf{q}\| = \left(\sum_{K\in\mathcal{T}_h} \|\mathbf{q}\|_{0,K}^2\right)^{1/2}.$$

Moreover, we define the H^ℓ-norm for a real-valued function u on the whole computational domain Ω as

$$\|u\|_{\Gamma_h} = \left(\sum_{K \in \mathcal{T}_h} \|u\|^2_{\Gamma_K} \right)^{1/2}.$$

Finally, we define the semi-norm on the element K and the semi-norm on the computational domain Ω as

$$|u|_{\ell,K} = \left(\sum_{\alpha+\beta=\ell} \left\| \frac{\partial^{\alpha+\beta} u}{\partial x^\alpha \partial y^\beta} \right\|^2_{0,K} \right)^{1/2}, \quad |u|_\ell = \left(\sum_{K \in \mathcal{T}_h} |u|^2_{\ell,K} \right)^{1/2}.$$

2.3. Preliminaries and Projections. In this subsection, we study the basic properties of the finite element space V_h^p. We first summarize some classical inverse properties in the following lemma [32].

Lemma 2.1. *Let $K = I_i \times J_j$ be an element in $\mathcal{T}_h$ and denote its boundary by Γ. Suppose that $v \in V_h^p$. Then there exists a constant C independent of the mesh size h and v such that*

$$\|\nabla v\|_{0,K} \leq C h^{-1} \|v\|_{0,K}, \tag{5a}$$

$$h \|v\|_{\infty,K} + h^{1/2} \|v\|_{0,\Gamma} \leq C \|v\|_{0,K}, \tag{5b}$$

where $\|v\|_{0,\Gamma} = \left(\int_\Gamma v^2(x(s), y(s))\, ds \right)^{1/2}$ and $\|v\|_{\infty,K} = \max\limits_{(x,y)\in K} |v(x,y)|$.

In this paper, we consider several special projections in one and two dimensions. We use $\mathbb{P}^p(I_i)$ to denote the space of polynomials of degree not exceeding p on $I_i = [x_{i-1}, x_i]$. Suppose $u \in L^2(I_i)$, then we define the standard L^2-projection, P_x, from $L^2(I_i)$ into V_h^p by

$$\int_{I_i} (u - P_x u) v \, dx = 0, \quad \forall\, v \in \mathbb{P}^p(I_i), \quad i = 1, 2, \ldots, n. \tag{6}$$

In addition, we also define two one-dimensional Gauss-Radau projections P_x^- and P_x^+. These special projections are used in the error estimates of the DG methods to derive optimal L^2-error bounds in the literature, e.g., in [15]. For $p \geq 1$, the Gauss-Radau projection $P_x^- u$ is defined by the following conditions

(7a)

$$\int_{I_i} (u - P_x^- u) v \, dx = 0, \ \forall\, v \in \mathbb{P}^{p-1}(I_i) \quad \text{and} \quad (u - P_x^- u)(x_i^-) = 0, \quad i = 0, 1, \ldots, n.$$

Similarly, the projection $P_x^+ u$ is defined by the following conditions

(7b)

$$\int_{I_i} (u - P_x^+ u) v \, dx = 0, \ \forall\, v \in \mathbb{P}^{p-1}(I_i) \quad \text{and} \quad (u - P_x^+ u)(x_{i-1}^+) = 0, \quad i = 0, 1, \ldots, n.$$

For the above one-dimensional projections, the following *a priori* error estimates hold

$$\begin{aligned} &\|u - P_x u\| + h \|(u - P_x u)'\| \leq C h^{p+1} \|u\|_{p+1}, \\ &\left\|u - P_x^\pm u\right\| + h \left\|(u - P_x^\pm u)'\right\| \leq C h^{p+1} \|u\|_{p+1}, \end{aligned} \tag{8}$$

where $\|w\| = \left(\sum_{i=1}^n \int_{I_i} w^2(x) dx \right)^{1/2}$ is the L^2-norm of $w(x)$ on the whole domain $I = [a, b]$.

Since Cartesian meshes are used in this paper, we apply the tensor product of the

projections in the one-dimensional case. On the rectangle element $K = I_i \times J_j$, we define the projections P_h^- and P_h^+ for a real-valued function $u = u(x, y)$ into V_h^p as tensor product of the projections in one dimension [34]

$$P_h^{\pm} u = P_x^{\pm} \otimes P_y^{\pm} u, \tag{9}$$

with the subscripts x and y indicating the use of the one-dimensional projections $P_x^{\pm}$ with respect to the corresponding variable. To be more specific, the projection $P_h^- u \in V_h^p$ can de obtained from the following conditions [52]:

$$\iint_K (u - P_h^- u) v \, dxdy = 0, \quad \forall\ v \in \mathbb{Q}^{p-1}(K), \tag{10a}$$

$$\int_{J_j} (u - P_h^- u)(x_i^-, y) v(y) \, dy = 0, \quad \forall\ v \in \mathbb{P}^{p-1}(J_j), \tag{10b}$$

$$\int_{I_i} (u - P_h^- u)(x, y_j^-) v(x) \, dx = 0, \quad \forall\ v \in \mathbb{P}^{p-1}(I_i), \tag{10c}$$

$$(u - P_h^- u)(x_i^-, y_j^-) = 0. \tag{10d}$$

We need another special projection $\mathbf{P}_h^+$ for vector-valued function $\mathbf{q} = [q_1, q_2]^t$. It is defined as follows [34]

$$\mathbf{P}_h^+ \mathbf{q} = [P_x^+ \otimes P_y q_1, P_x \otimes P_y^+ q_2]^t, \tag{11}$$

where P_x and P_x^+ are the one-dimensional L^2- and Gauss-Radau projections in the x-direction, respectively. Similarly, P_y and P_y^+ are the one-dimensional L^2- and Gauss-Radau projections in the y-direction, respectively. We remark that the projection $\mathbf{P}_h^+ \mathbf{q} \in \mathbf{V}_h^p$ has the following properties

$$\iint_K (\mathbf{P}_h^+ \mathbf{q} - \mathbf{q}) \cdot \nabla v \, dxdy = 0 \quad \text{and} \quad \int_{\Gamma^-} \mathbf{n} \cdot (\mathbf{P}_h^+ \mathbf{q} - \mathbf{q})^+ v^+ ds = 0 \quad \forall\ v \in \mathcal{Q}^p(K). \tag{12}$$

We note that the projection $\mathbf{P}_h^+ \mathbf{q}$ is uniquely defined by the conditions (12).

For the above two-dimensional projections, we have the following projection results [34].

Lemma 2.2. *The two-dimensional projections P_h^- and $\mathbf{P}_h^+$ are well-defined. Furthermore, for $u \in H^{p+1}(\Omega)$ and $\mathbf{q} \in \left(H^{p+1}(\Omega)\right)^2$, there exists a constant C independent of h such that*

$$\left\|u - P_h^- u\right\| + h \left\|u - P_h^- u\right\|_{\infty} \le C h^{p+1} \|u\|_{p+1}, \quad \left\|\mathbf{q} - \mathbf{P}_h^+ \mathbf{q}\right\| \le C h^{p+1} \|\mathbf{q}\|_{p+1}. \tag{13}$$

2.4. *A priori* error estimates. In this section, we recall the *a priori* error estimates of the LDG method from [25]. From now on, the symbol C (with or without subscripts) will be used to denote a generic positive constant independent of the mesh size h. However, all constants may depend on the exact solution u of (1). Also, the constants may take different values at different places.

To derive the error estimates, let us first denote the errors by

$$e_u = u - u_h, \qquad \mathbf{e}_{\mathbf{q}} = \mathbf{q} - \mathbf{q}_h.$$

We denote the error between the LDG solutions and the projections of the exact solutions by

$$\bar{e}_u = P_h^- u - u_h \in V_h^p, \quad \bar{\mathbf{e}}_{\mathbf{q}} = \mathbf{P}_h^+ \mathbf{q} - \mathbf{q}_h \in \mathbf{V}_h^p.$$

We denote the projection errors by

$$\epsilon_u = u - P_h^- u, \quad \boldsymbol{\epsilon}_{\mathbf{q}} = \mathbf{q} - \mathbf{P}_h^+ \mathbf{q}.$$

We remark that the actual errors e_u and $\mathbf{e_q}$ can be decomposed as

$$e_u = \bar{e}_u + \epsilon_u, \quad \mathbf{e_q} = \bar{\mathbf{e}}_\mathbf{q} + \boldsymbol{\epsilon}_\mathbf{q}. \tag{14}$$

In the next theorem, we summarize the *a priori* error estimates for e_u and $\mathbf{e_q}$ in the L^2-norm.

Theorem 2.1. *Suppose that $u \in H^{p+2}(\Omega)$ is the exact solution of (1). Let $\mathbf{q} = \nabla u \in \left(H^{p+1}(\Omega)\right)^2$. Let $p \geq 1$ and assume that $(u_h, \mathbf{q}_h)$ are the LDG solutions defined in (4). Then, for sufficiently small h, there exists a constant C independent of h such that*

$$\|e_u\| \leq Ch^{p+1}. \tag{15}$$

$$\|\mathbf{e_q}\| \leq Ch^{p+1}. \tag{16}$$

Proof. Cf. [25, Theorem 2]. □

Remark 2.2. *We would like to mention that in* [34]*, Cockburn* et al.*, presented a superconvergence result for the LDG method for the linear elliptic problem (1), but $f(\mathbf{x}, u)$ is linear in u, on Cartesian grids. They identified a special numerical flux for which the L^2-norm of the gradient and the L^2-norm of the potential are of orders $p+1/2$ and $p+1$, respectively, when tensor product polynomials of degree at most p are used. In* [25, Theorem 2]*, we proved optimal results for the semilinear case.*

3. Superconvergence error analysis

In this section, we investigate the superconvergence properties of the LDG method presented in Section 2. We prove that the LDG solution u_h is superconvergent with order $p+2$ towards the Gauss-Radau interpolant of the exact solution πu. We use this new superconvergence result to prove that the LDG error e_u can be decomposed into two errors. The first is the significant part of the error which is a linear combination of two $(p+1)$-degree Radau polynomials in the x- and y- directions. The second part is less significant and it converges to zero in the L^2-norm with order $p+2$.

We first recall the following superconvergence results from [25].

Theorem 3.1. *Under the assumptions of Theorem 2.1, there exists a positive constant C independent of mesh size h such that*

$$\|\bar{e}_u\| \leq Ch^{p+2}. \tag{17}$$

$$\|\bar{\mathbf{e}}_\mathbf{q}\| \leq Ch^{p+2}. \tag{18}$$

Proof. Cf. [25, Theorems 3, 4]. □

Before, we present our main superconvergence results, we define the Legendre and Radau polynomials.

Legendre polynomials on the reference interval $[-1, 1]$ can be defined recursively by

$$\tilde{L}_0(\xi) = 1, \quad \tilde{L}_1(\xi) = \xi, \quad p\tilde{L}_p(\xi) = (2p-1)\tilde{L}_{p-1}(\xi) - (p-1)\tilde{L}_{p-2}(\xi), \quad \xi \in [-1, 1].$$

The pth-degree Legendre polynomial satisfies the following useful properties:

(19)
$$\hat{L}_p(-1) = (-1)^p, \quad \hat{L}_p(1) = 1, \quad \hat{L}'_p(-1) = (-1)^{p+1}\frac{p(p+1)}{2}, \quad \hat{L}'_p(1) = \frac{p(p+1)}{2},$$

(20)
$$\int_{-1}^{1} \hat{L}_p(\xi)\hat{L}_q(\xi)d\xi = \frac{2}{2p+1}\delta_{pq},$$

where δ_{pq} is used to denote the Kronecker symbol.

The $(p+1)$-degree right Radau polynomial on the reference interval $[-1,1]$ is defined by

$$\hat{R}_{p+1}(\xi) = \hat{L}_{p+1}(\xi) - \hat{L}_p(\xi), \quad \xi \in [-1,1]. \tag{21}$$

It can be showing that $\hat{R}_{p+1}(\xi),\ \xi \in [-1,1]$ has $p+1$ distinct real roots in $[-1,1]$. We will denote them by $-1 < \xi_0 < \xi_1 < \cdots < \xi_p = 1$.

Using the change of variables

$$x(\xi) = \frac{x_i + x_{i-1}}{2} + \frac{h_i}{2}\xi, \quad y(\eta) = \frac{y_j + y_{j-1}}{2} + \frac{k_j}{2}\eta, \quad \xi,\ \eta \in [-1,1], \tag{22}$$

we get the p-degree shifted Legendre polynomials on the physical intervals I_i and J_j

$$L_{p,i}(x) = \hat{L}_p\left(\frac{2x - x_i - x_{i-1}}{h_i}\right),\ L_{p,j}(y) = \hat{L}_p\left(\frac{2y - y_j - y_{j-1}}{k_j}\right),\ x \in I_i,\ y \in J_j.$$

Similarly, the p-degree shifted right Radau polynomials on I_i and J_j are given by

$$R_{p,i}(x) = \hat{R}_p\left(\frac{2x - x_i - x_{i-1}}{h_i}\right),\ R_{p,j}(y) = \hat{R}_p\left(\frac{2y - y_j - y_{j-1}}{k_j}\right),\ x \in I_i,\ y \in J_j.$$

Next, we recall some results which will be needed in the *a posteriori* error analysis.

Lemma 3.1. *The shifted Legendre and Radau polynomials on I_i and J_j satisfy the following properties*

$$\|L_{p,i}\|^2_{0,I_i} = \frac{h_i}{2p+1}, \tag{23a}$$

$$\int_{I_i} R'_{p+1,i}(x)L_{p,i}(x)dx = \int_{J_j} R'_{p+1,j}(y)L_{p,j}(y)dy = 2, \tag{23b}$$

$$\|R_{p+1,i}\|^2_{0,I_i} = \frac{4(p+1)}{(2p+1)(2p+3)}h_i, \quad \|R_{p+1,j}\|^2_{0,J_j} = \frac{4(p+1)}{(2p+1)(2p+3)}k_j, \tag{23c}$$

where $h_i = x_i - x_{i-1}$ and $k_i = y_j - y_{j-1}$.

Proof. The proof of this lemma can be found in [11] more precisely in its Lemma 2.1. □

Next, we define an important two-dimensional interpolating right Radau polynomial $\pi u \in V_h^p$ as follows: on each rectangular element $K = [x_{i-1}, x_i] \times [y_{j-1}, y_j] = I_i \times J_j$, the polynomial $\pi u \in \mathcal{Q}^p(K)$ interpolates $u(x,y)$ at the $(p+1)^2$ points $(x_{i,k}, y_{j,l})$, $k,l = 0,1,\ldots,p$, *i.e.*,

$$\pi u(x_{i,k}, y_{j,l}) = u(x_{i,k}, y_{j,l}),\ k,l = 0,1,\ldots,p,$$

where $x_{i,k}$ and $y_{j,l}$ are, respectively, the roots of $R_{p+1,i}(x),\ x \in I_i$ and $R_{p+1,j}(y),\ y \in J_j$.

In the next lemma, we show that the interpolation error $u - \pi u$ on each element K can be split into a significant part and a less significant part.

Lemma 3.2. *Suppose that $u \in H^{p+2}(K)$. Then the interpolation error $u - \pi u$ can be split as*

$$u - \pi u = \phi + \gamma, \quad (x,y) \in K = I_i \times J_j, \tag{24a}$$

where the significant part, ϕ, is a linear combination of two $(p+1)$-degree right Radau polynomials in the x- and y-directions i.e.,

$$\phi = a_i R_{p+1,i}(x) + b_j R_{p+1,j}(y), \tag{24b}$$

and the less significant part $\gamma = u - \hat{\pi} u$, where for each $K \in \mathcal{T}_h$, $\hat{\pi} u \in \mathcal{Q}^p(K) \cup span(\{x^{p+1}, y^{p+1}\})$ is the two-dimensional interpolation polynomial that interpolates u at the Radau points $(x_{i,k}, y_{j,l})$, $k,l = 0, 1, \ldots, p$ and at the two additional points (x_{i-1}, y_j) and (x_i, y_{j-1}). Moreover, it satisfies the following estimate

$$\|\gamma\|_{s,K} \leq C h^{p+2-s} \|u\|_{p+2,K}, \ 0 \leq s \leq p+1. \tag{24c}$$

Finally, we have the following estimate

$$\|\phi\|_{s,K} \leq C h^{p+1-s} \|u\|_{p+2,K}, \ 0 \leq s \leq p. \tag{24d}$$

Proof. The proof of lemma can be found in [16] more precisely in its Lemma 3.2. □

In [16], we proved that the error between πu and $P_h^- u$ converges to zero in the L^2-norm and the order of convergence is $p+2$. We present this result in the following lemma.

Lemma 3.3. *Assume that $u \in H^{p+2}(\Omega)$. Let $P_h^- u$ be the two-dimensional Gauss-Radau projection and πu be the two-dimensional Radau interpolating polynomial. Then, we have the following superconvergence property*

$$\left\| \pi u - P_h^- u \right\| \leq C h^{p+2} \|u\|_{p+2}. \tag{25}$$

Proof. The proof of (25) can be found in [16] more precisely in its Lemma 3.3. □

Now, we are ready to prove our main superconvergence results. More specifically, we prove that the significant part of the actual error e_u is a linear combination of two $(p+1)$-degree right Radau polynomials in the x- and y- directions.

Theorem 3.2. *Suppose that the assumptions of Theorem 2.1 are satisfied. Then there exists a constant C independent of h such that*

$$\|u_h - \pi u\| \leq C h^{p+2}. \tag{26}$$

Moreover, on each element, the error can be decomposed as

$$e_u(x,y) = \phi(x,y) + \omega(x,y), \quad \forall \ (x,y) \in K \in \mathcal{T}_h, \tag{27a}$$

where

$$\phi = a_i R_{p+1,i}(x) + b_j R_{p+1,j}(y), \quad \omega = \gamma + \pi u - u_h, \tag{27b}$$

and

$$\|\omega\|_s \leq C h^{p+2-s}, \quad s = 0, 1. \tag{27c}$$

Proof. We write the interpolation error $u_h - \pi u$ as adding and subtracting $P_h^- u$ as

$$u_h - \pi u = (u_h - P_h^- u) + (P_h^- u - \pi u) = -\bar{e}_u + (P_h^- u - \pi u).$$

Taking the L^2-norm and applying the Cauchy-Schwarz inequality, we obtain

$$\|u_h - \pi u\| \leq \|\bar{e}_u\| + \left\| P_h^- u - \pi u \right\|.$$

Using the superconvergence results (17) and (25), we deduce (26).

Next, we split the error e_u by adding and subtracting the interpolating polynomial πu as

$$e_u = u - u_h = (u - \pi u) + (\pi u - u_h).$$

Since on each element K the interpolation error can be split as $u - \pi u = \phi + \gamma$, we have

$$e_u = (\phi + \gamma) + (\pi u - u_h) = \phi + (\gamma + \pi u - u_h) = \phi + \omega, \tag{28a}$$

where $\phi = a_i R_{p+1,i}(x) + b_j R_{p+1,j}(y)$ and ω is given by

$$\omega = \gamma + \pi u - u_h = u - \hat{\pi} u + \pi u - u_h. \tag{28b}$$

Finally, we will derive (27c). Using the triangle inequality and the classical inequality $(a+b)^2 \leq 2(a^2+b^2)$, we get

$$\begin{aligned} \|\omega\|_{s,K}^2 = \|\gamma + (\pi u - u_h)\|_{s,K}^2 &\leq \left(\|\gamma\|_{s,K} + \|\pi u - u_h\|_{s,K} \right)^2 \\ &\leq 2 \left(\|\gamma\|_{s,K}^2 + \|\pi u - u_h\|_{s,K}^2 \right). \end{aligned}$$

Since $\pi u - u_h \in V_h^p$, we can use the inverse inequality to have

$$\|\pi u - u_h\|_{s,K} \leq C_0 h^{-s} \|\pi u - u_h\|_{0,K}, \quad s = 0, 1.$$

Thus, we obtain

$$\|\omega\|_{s,K}^2 \leq 2 \left(\|\gamma\|_{s,K}^2 + C_0^2 h^{-2s} \|\pi u - u_h\|_{0,K}^2 \right).$$

Summing over all elements $K \in \mathcal{T}_h$ and using the estimates (24c) and (26) yields

$$\begin{aligned} \|\omega\|_s^2 = \sum_{K \in \mathcal{T}_h} \|\omega\|_{s,K}^2 &\leq 2 \left(\sum_{K \in \mathcal{T}_h} \|\gamma\|_{s,K}^2 + C_0^2 h^{-2s} \sum_{K \in \mathcal{T}_h} \|\pi u - u_h\|_{0,K}^2 \right) \\ &\leq 2 \left(C_1 h^{2p+4-2s} + C_0^2 C_2 h^{2p+4-2s} \right) \leq C h^{2p+4-2s}, \end{aligned}$$

which complete the proof of (27c). □

4. *A posteriori* error estimation

As opposed to *a priori* error estimates (15) and (16), *a posteriori* error estimates are computable quantities in terms of the numerical solution. They measure the actual errors without the knowledge of the exact solutions. Accurate error estimation is a critical component of numerical simulations, being useful for reliability, uncertainty quantification and adaptive error control.

In this section, we present a residual-based *a posteriori* error estimation procedure to estimate the LDG error $e_u = u - u_h$. We then use the superconvergence results from the previous section to prove that these *a posteriori* error estimates converge to the true error e_u in the L^2-norm under mesh refinement with order $p+2$. Finally, we prove that the global effectivity index, which is the ratio between the *a posteriori* error estimator and the exact error in the L^2-norm, converge to unity as $h \to 0$.

We first derive a formulation to estimate the error e_u. Multiplying (2b) by a test function $\mathbf{r} \in \mathbf{V}_h^p$ and integrating over an arbitrary rectangle K of the mesh, we get

$$\iint_K \nabla u \cdot \mathbf{r} \, dxdy = \iint_K \mathbf{q} \cdot \mathbf{r} \, dxdy. \tag{29}$$

Replacing u by $u_h + e_u$ and $\mathbf{q}$ by $\mathbf{q}_h + \mathbf{e_q}$ and rearranging terms, we obtain

$$\iint_K \nabla e_u \cdot \mathbf{r}\, dxdy = -\iint_K (\nabla u_h - \mathbf{q}_h - \mathbf{e_q}) \cdot \mathbf{r}\, dxdy. \tag{30}$$

Decomposing the error e_u as in (27a) gives the weak formulation

$$\iint_K \nabla \phi \cdot \mathbf{r}\, dxdy = -\iint_K (\nabla u_h - \mathbf{q}_h + \nabla \omega - \mathbf{e_q}) \cdot \mathbf{r}\, dxdy.$$

Taking the test function $\mathbf{r} = [L_{p,i}(x), 0]^t$ and $\mathbf{r} = [0, L_{p,j}(y)]^t$ and applying (27b) *i.e*, $\phi = a_i R_{p+1,i}(x) + b_j R_{p+1,j}(y)$, we get the two linear system of equations

$$\begin{aligned} a_i \iint_K R'_{p+1,i}(x) L_{p,i}(x)\, dxdy &= -\iint_K \left((u_h)_x - q_{1,h} + \omega_x - e_{q_1}\right) L_{p,i}(x)\, dxdy, \\ b_j \iint_K R'_{p+1,j}(y) L_{p,j}(y)\, dxdy &= -\iint_K \left((u_h)_y - q_{2,h} + \omega_y - e_{q_2}\right) L_{p,j}(y)\, dxdy. \end{aligned}$$

Using the property (23b) and solving for the constants a_i and b_j, we find

$$a_i = -\frac{1}{2k_j} \iint_K \left((u_h)_x - q_{1,h} + \omega_x - e_{q_1}\right) L_{p,i}(x)\, dxdy, \tag{31a}$$

$$b_j = -\frac{1}{2h_i} \iint_K \left((u_h)_y - q_{2,h} + \omega_y - e_{q_2}\right) L_{p,j}(y)\, dxdy. \tag{31b}$$

We remark that a_i and b_j are not computable quantities since ω and $\mathbf{e_q}$ are generally unknown terms. For this, we propose the following error estimation procedure: We approximate the actual error $e_u(x, y)$ on each rectangle $K \in \mathcal{T}_h$ by the leading part, denoted by $E_u(x, y)$, as

$$\boxed{E_u(x, y) = \hat{a}_i R_{p+1,i}(x) + \hat{b}_j R_{p+1,j}(y), \quad \forall\ (x, y) \in K,} \tag{32a}$$

where the modified coefficients $\hat{a}_i$ and $\hat{b}_j$ are approximations of the coefficients a_i and b_j, respectively. These computable coefficients $\hat{a}_i$ and $\hat{b}_j$ are obtained from the coefficients a_i and b_j by neglecting the unknown quantities $\mathbf{e_q}$ and ω *i.e*.,

$$\boxed{\hat{a}_i = -\frac{1}{2k_j} \iint_K \left((u_h)_x - q_{1,h}\right) L_{p,i}(x)\, dxdy,} \tag{32b}$$

$$\boxed{\hat{b}_j = -\frac{1}{2h_i} \iint_K \left((u_h)_y - q_{2,h}\right) L_{p,j}(y)\, dxdy.} \tag{32c}$$

We remark that the proposed LDG error estimator $E_u(x, y) = \hat{a}_i R_{p+1,i}(x) + \hat{b}_j R_{p+1,j}(y)$, $\forall\ (x, y) \in K$ depends on the LDG solution $(u_h, \mathbf{q}_h)$ solely. Therefore, it is a computable quantity. In addition, the local error estimator $E_u(x, y)$, $\forall\ (x, y) \in K \in \mathcal{T}_h$ is computationally simple since it is derived by solving a local linear problem with no boundary conditions on each element $K \in \mathcal{T}_h$.

In order to evaluate the accuracy of our error estimator, we use the global effectivity index in the L^2-norm defined by

$$\Theta = \frac{\|E_u\|}{\|e_u\|} = \left(\frac{\sum\limits_{K \in \mathcal{T}_h} \|E_u\|^2_{0,K}}{\sum\limits_{K \in \mathcal{T}_h} \|e_u\|^2_{0,K}} \right)^{1/2},$$

with $\|E_u\|$ denoting an estimate for the actual error $\|e_u\|$ in the L^2-norm. The global effectivity index represents the degree of over or under estimation and should be ideally close to 1.0.

In the next theorem, we prove that the error estimator E_u converges to the exact error e_u in the L^2-norm under h-refinement.

Theorem 4.1. *Assume that the conditions of Theorem 2.1 are satisfied. Suppose that (a_i, b_j) and $(\hat{a}_i, \hat{b}_j)$ are, respectively, the coefficients defined by (31) and (32). If the error estimator $E_u(x, y)$ is given by (32a), then*

$$\|e_u - E_u\| \leq Ch^{p+2}. \tag{33}$$

Moreover, we have

$$\|E_u\| - Ch^{p+2} \leq \|e_u\| \leq \|E_u\| + Ch^{p+2}. \tag{34}$$

Finally, under the assumption

$$\|e_u\| \geq Ch^{p+1}, \tag{35}$$

the global effectivity index $\Theta = \frac{\|E_u\|}{\|e_u\|}$ converges to unity at $\mathcal{O}(h)$ rate i.e.,

$$\Theta = 1 + \mathcal{O}(h). \tag{36}$$

Proof. We begin the proof of the estimate (33). For $(x, y) \in K \in \mathcal{T}_h$, we have

$$\begin{aligned} e_u(x, y) &= a_i R_{p+1,i}(x) + b_j R_{p+1,j}(y) + \omega(x, y), \\ E_u(x, y) &= \hat{a}_i R_{p+1,i}(x) + \hat{b}_j R_{p+1,j}(y). \end{aligned}$$

Subtracting E_u from e_u and taking the L^2-norm, we get

$$\|e_u - E_u\|_{0,K}^2 = \iint_K \Big((a_i - \hat{a}_i)R_{p+1,i}(x) + (b_j - \hat{b}_j)R_{p+1,j}(y) + \omega(x, y)\Big)^2 \, dxdy.$$

Applying the inequality $(a + b + c)^2 \leq 3(a^2 + b^2 + c^2)$, we obtain

$$\|e_u - E_u\|_{0,K}^2 \leq 3(a_i - \hat{a}_i)^2 \|R_{p+1,i}\|_{0,K}^2 + 3(b_j - \hat{b}_j)^2 \|R_{p+1,j}\|_{0,K}^2 + 3\|\omega\|_{0,K}^2 .$$

Using the estimate (23c), we get

$$\|e_u - E_u\|_{0,K}^2 \leq \frac{12(p+1)h_i k_j}{(2p+1)(2p+3)} \Big((a_i - \hat{a}_i)^2 + (b_j - \hat{b}_j)^2\Big) + 3\|\omega\|_{0,K}^2 . \tag{37}$$

Next, we will estimate $(a_i - \hat{a}_i)^2 + (b_j - \hat{b}_j)^2$. Subtracting (32) from (31), we obtain

$$\begin{aligned} a_i - \hat{a}_i &= -\frac{1}{2k_j} \iint_K (\omega_x - e_{q_1}) \, L_{p,i}(x) \, dxdy, \\ b_j - \hat{b}_j &= -\frac{1}{2h_i} \iint_K (\omega_y - e_{q_2}) \, L_{p,j}(y) \, dxdy. \end{aligned}$$

Squaring both sides and using the inequality $(a - b)^2 \leq 2(a^2 + b^2)$, we get

$$\begin{aligned} (a_i - \hat{a}_i)^2 &\leq \frac{1}{2k_j^2} \left(\left(\iint_K \omega_x L_{p,i}(x) \, dxdy \right)^2 + \left(\iint_K e_{q_1} L_{p,i}(x) \, dxdy \right)^2 \right), \\ (b_j - \hat{b}_j)^2 &\leq \frac{1}{2h_i^2} \left(\left(\iint_K \omega_y L_{p,j}(y) \, dxdy \right)^2 + \left(\iint_K e_{q_2} L_{p,j}(y) \, dxdy \right)^2 \right). \end{aligned}$$

Applying the Cauchy-Schwarz inequality and applying (23a) yields

$$\begin{aligned}(a_i-\hat{a}_i)^2 \leq & \frac{1}{2k_j^2}\left(\|\omega_x\|_{0,K}^2+\|e_{q_1}\|_{0,K}^2\right)\|L_{p,i}\|_{0,K}^2\\ = & \frac{h_i}{2(2p+1)k_j}\left(\|\omega_x\|_{0,K}^2+\|e_{q_1}\|_{0,K}^2\right),\\ (b_j-\hat{b}_j)^2 \leq & \frac{1}{2h_i^2}\left(\|\omega_y\|_{0,K}^2+\|e_{q_2}\|_{0,K}^2\right)\|L_{p,j}\|_{0,K}^2\\ = & \frac{k_j}{2(2p+1)h_i}\left(\|\omega_y\|_{0,K}^2+\|e_{q_2}\|_{0,K}^2\right).\end{aligned}$$

Adding both equations, we get

$$\begin{aligned}(a_i-\hat{a}_i)^2+(b_j-\hat{b}_j)^2 \leq & \frac{h_i}{2(2p+1)k_j}\left(\|e_{q_1}\|_{0,K}^2+\|\omega_x\|_{0,K}^2\right)\\ & +\frac{k_j}{2(2p+1)h_i}\left(\|e_{q_2}\|_{0,K}^2+\|\omega_y\|_{0,K}^2\right).\end{aligned} \tag{38}$$

Combining (37) and (38), we arrive at

$$\begin{aligned}\|e_u-E_u\|_{0,K}^2 \leq & \frac{6(p+1)}{(2p+1)^2(2p+3)}\left(h_i^2\|e_{q_1}\|_{0,K}^2+k_j^2\|e_{q_2}\|_{0,K}^2+h_i^2\|\omega_x\|_{0,K}^2\right.\\ & \left.+k_j^2\|\omega_y\|_{0,K}^2\right)+3\|\omega\|_{0,K}^2\\ \leq & \frac{6(p+1)h^2}{(2p+1)^2(2p+3)}\left(\|\mathbf{e_q}\|_{0,K}^2+\|\nabla\omega\|_{0,K}^2\right)+3\|\omega\|_{0,K}^2\\ \leq & C_p\left(h^2\|\mathbf{e_q}\|_{0,K}^2+h^2\|\nabla\omega\|_{0,K}^2+\|\omega\|_{0,K}^2\right).\end{aligned}$$

where $C_p=\max\left(3,\frac{6(p+1)}{(2p+1)^2(2p+3)}\right)$. Since $\|\nabla\omega\|_{0,K}\leq\|\omega\|_{1,K}$, we deduce

$$\|e_u-E_u\|_{0,K}^2 \leq C_p\left(h^2\|\mathbf{e_q}\|_{0,K}^2+h^2\|\omega\|_{1,K}^2+\|\omega\|_{0,K}^2\right),$$

Summing over all elements and applying the estimates (16) and (27c), we arrive at

$$\begin{aligned}\|e_u-E_u\|^2 \leq & C_p\left(h^2\|\mathbf{e_q}\|^2+h^2\|\omega\|_1^2+\|\omega\|^2\right)\\ \leq & C_p\left(h^2C_1h^{2p+2}+h^2C_2h^{2p+2}+C_3h^{2p+4}\right)\leq Ch^{2p+4},\end{aligned}$$

which completes the proof of (33).

To show (34), we apply the reverse triangle inequality as

$$|\|E_u\|-\|e_u\||\leq\|E_u-e_u\|. \tag{39}$$

Combining (33) and (39), we establish (34).

Finally, we prove (36). Dividing (39) by $\|e_u\|$ and using the estimate (33) and the assumption (35), we get

$$|\Theta-1|=\left|\frac{\|E_u\|}{\|e_u\|}-1\right|=\frac{|\|E_u\|-\|e_u\||}{\|e_u\|}\leq\frac{\|E_u-e_u\|}{\|e_u\|}\leq\frac{C_1h^{p+2}}{C_2h^{p+1}}\leq Ch,$$

which gives $\Theta=1+\mathcal{O}(h)$. Thus, we completed the proof of the Theorem. □

Theorem 4.1 indicates that the *a posteriori* error estimate E_u converges to the true error e_u at $\mathcal{O}(h^{p+2})$ rate in the L^2-norm. It also suggests that the global effectivity index Θ converges to unity at $\mathcal{O}(h)$ rate as $h\to 0$.

Remark 4.1. The error estimator η_u is said to be reliable (respectively efficient) if there exists a constant $C_{\rm rel}$ (respectively $C_{\rm eff}$), independent of the mesh size h, such that

$$C_{\rm eff}\ \eta_u + \text{H.O.T} \le \|e_u\| \le C_{\rm rel}\ \eta_u + \text{H.O.T},$$

where H.O.T is a higher order term. Therefore, the estimate (34) indicates that the proposed error estimator $\eta_u = \|E_u\| = \left(\sum_{K\in\mathcal{T}_h} \|E_u\|^2_{0,K} \right)^{1/2}$ is reliable and efficient.

Remark 4.2. Since $e_u = u - u_h$, we have by the estimate (33)

$$\|u - (u_h + E_u)\| = \|(u - u_h) - E_u\| = \|e_u - E_u\| \le Ch^{p+2}.$$

Consequently, the post-processed approximation $\hat{u}_h = u_h + E_u$ yields $\mathcal{O}(h^{p+2})$ superconvergent solution.

Remark 4.3. The performance of an error estimator is commonly measured by the effectivity index which is the ratio of the estimated error to the actual error. In particular, we say that the error estimator is asymptotically exact if the effectivity index approaches unity as the mesh size goes to zero. We note that (36) indicates that the computable quantity $\|E_u\|$ provides an asymptotically exact *a posteriori* estimator on the actual error $\|e_u\|$.

Remark 4.4. The assumption (35) implies that terms of order $\mathcal{O}(h^{p+1})$ are present in the error $\|e_u\|$. If this were not the case, the error estimate $\|E_u\|$ might not be such a good approximation of the actual error $\|e_u\|$. Even though the proof of (36) is valid under the assumption (35), our computational results given in the next section suggest that the global effectivity index in the L^2-norm converge to unity at $\mathcal{O}(h^2)$ rate. Thus, the proposed error estimation procedure is an excellent measure of the gradient of the error.

Remark 4.5. We note that E_u is a computable quantity since it only depends on the LDG solution $(u_h, \mathbf{q}_h)$. It provides an *a posteriori* estimator on the error $\|u - u_h\|$. We would like to emphasize that our LDG error estimate is computationally simple and is obtained by solving a local problem with no boundary conditions on each element.

Remark 4.6. *In our error analysis p is assumed to be ≥ 1. When $p = 0$, the superconvergence results in this paper and in* [25] *are not valid. Also, our error estimate procedure does not apply when $p = 0$.*

5. Numerical examples

In this section we present several numerical examples to validate the theoretical results and test the performance of the residual-type *a posteriori* error estimator. We use the same test problems in [25] where we showed the L^2 errors $\|e_u\| = \mathcal{O}(h^{p+1})$, $\|\mathbf{e_q}\| = \mathcal{O}(h^{p+1})$, $\|\bar{e}_u\| = \mathcal{O}(h^{p+2})$, $\|\bar{\mathbf{e}}_\mathbf{q}\| = \mathcal{O}(h^{p+2})$, and $\|\nabla\bar{e}_u\| = \mathcal{O}(h^{p+1})$. Here, we will show the convergence of the errors $\|u_h - \pi u\|$, $\|e_u - E_u\|$, and $|\Theta - 1|$ on logarithmic scales. The numerical convergence order of the error is computed by using the formula

$$\text{order} = -\frac{\ln(e_{n_1}/e_{n_2})}{\ln(n_1/n_2)},$$

where e_{n_k}, $k = 1, 2$, is the error using $N_k = n_k^2$ square elements. We will consider problems with smooth solutions, but we will also consider problems that do not conform to the theory presented above, with a variety of exact solutions that are

less regular than $H^4(\Omega)$. When the Dirichlet boundary conditions are used, the stabilization parameter is given by $C_{11} = 1$, when tensor product polynomials of degree at most p are considered as basis for the LDG method.

Example 5.1. In the first example, we test the superconvergence results and demonstrate the robustness of the proposed residual-type *a posteriori* error estimator to the classical semilinear Poisson-Boltzmann (PB) equation

$$-u_{xx} - u_{yy} = e^{-u} + 8\pi^2 \sin(2\pi(x+y)) - e^{-\sin(2\pi(x+y))}, \ (x,y) \in [0,1]^2. \tag{40a}$$

The boundary conditions are extracted from the analytical solution

$$u(x,y) = \sin(2\pi(x+y)).$$

Several numerical tests are performed on this example to investigate the effect of boundary conditions. We will consider the purely Dirichlet boundary conditions, the mixed Dirichlet-Neumann boundary conditions, and finally the periodic boundary conditions. We first consider the Poisson-Boltzmann equation (40a) subject to the boundary conditions of Dirichlet type

$$u(x,0) = \sin(2\pi x), \ u(x,1) = \sin(2\pi x), \quad x \in [0,1], \tag{40b}$$

$$u(0,y) = \sin(2\pi y), \ u(1,y) = \sin(2\pi y), \quad y \in [0,1]. \tag{40c}$$

We solve this problem using the LDG scheme presented in Section 2 on a uniform Cartesian meshes having $N = 25$, 100, 225, 400, and 625 elements. These meshes are obtained by dividing the computational domain $\overline{\Omega} = [0,1]^2$ into n^2 squares with $n = 5$, 10, 15, 20, and 25. We compute the LDG solutions $u_h \in V_h^p$ and $\mathbf{q}_h \in \mathbf{V}_h^p$ with $p = 1, 2, 3, 4$. In the left figure of Figure 1, we show the L^2-norm of the errors between the LDG solution u_h and the right Radau interpolating polynomial πu. These results indicate that the LDG solution u_h is $\mathcal{O}(h^{p+2})$ superclose to to the interpolant πu in the L^2-norm for $p = 1, 2, 3, 4$. These results are in full agreement with the theoretical result of Theorem 3.2.

Next, we implement our error estimation procedure presented in Section 4 to find the error estimator E_u on each rectangle of the mesh and the global error $\|e_u - E_u\|$. In the right figure of Figure 1, we show the convergence orders of the global errors $\|e_u - E_u\|$. We observe that $\|e_u - E_u\| = \mathcal{O}(h^{p+2})$ as $h \to 0$. We conclude that our *a posteriori* error estimator E_u converges to the actual error e_u in the L^2-norm as $h \to 0$. This is in full agreement with the theoretical result presented in Theorem 4.1. This example shows that the orders of convergence derived in this paper are sharp.

Next, we present the global effectivity index Θ in Table 1. We observe that Θ is near unity and converges to unity under h-refinement. Finally, the errors $|\Theta - 1|$ and their orders of convergence shown in the same Table 1 suggest that $|\Theta - 1|$ is $\mathcal{O}(h^2)$. This numerical convergence rate is higher than the theoretical rate derived in Theorem 4.1 by one order.

We repeat the previous experiment with all parameters kept unchanged except that we use the mixed Dirichlet-Neumann boundary conditions

$$u(0,y) = \sin(2\pi y), \ u(x,0) = \sin(2\pi x), \tag{40d}$$

$$u_x(1,y) = \cos(2\pi y), \quad u_y(x,1) = \cos(2\pi x), \ (x,y) \in \partial\Omega. \tag{40e}$$

In the left figure of Figure 2, we report the L^2 errors between the LDG solution u_h and the right Radau interpolating polynomial πu and their convergence orders. Clearly, these results show optimal convergence orders. Again, our results are in full agreement with the theoretical results. The L^2 errors $\|e_u - E_u\|$ shown in the right

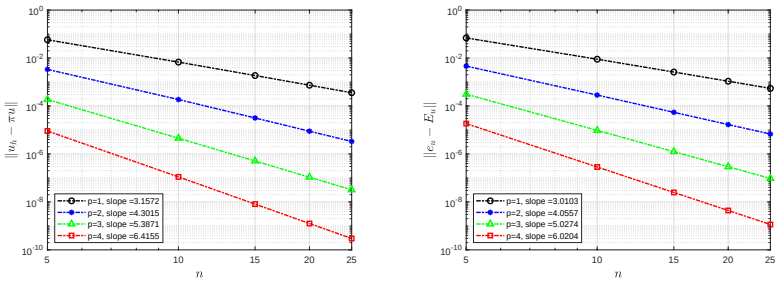

Figure 1: Convergence orders for $\|u_h - \pi u\|$ (left) and $\|e_u - E_u\|$ (right) for the B-VP (40a) subject to the Dirichlet boundary conditions (40b-40c) on uniform meshes having $N = 25$, 100, 225, 400, and 625 elements using the spaces $\mathcal{Q}^p,\ p = 1, 2, 3, 4$. The slopes of the fitting lines are shown on the graph.

TABLE 1. Global effectivity indices Θ and the errors $|\Theta - 1|$ for the BVP (40a) subject to the Dirichlet boundary conditions (40b-40c) on uniform meshes having $N = 25$, 100, 225, 400, and 625 elements using $\mathcal{Q}^p,\ p = 1, 2, 3, 4$.

N	$p=1$			$p=2$		
	Θ	$\lvert\Theta-1\rvert$	order	Θ	$\lvert\Theta-1\rvert$	order
25	0.80938	1.9062e-1		0.88485	1.1515e-1	
100	0.95013	4.9866e-2	1.9346	0.97392	2.6076e-2	2.1427
225	0.97849	2.1506e-2	2.0742	0.98970	1.0299e-2	2.2911
400	0.98844	1.1563e-2	2.1570	0.99462	5.3758e-3	2.2599
625	0.99291	7.0918e-3	2.1908	0.99672	3.2751e-3	2.2208
N	$p=3$			$p=4$		
	Θ	$\lvert\Theta-1\rvert$	order	Θ	$\lvert\Theta-1\rvert$	order
25	0.91800	8.2001e-2		0.91694	8.3063e-2	
100	0.98045	1.9550e-2	2.0685	0.98077	1.9230e-2	2.1108
225	0.99157	8.4280e-3	2.0752	0.99180	8.1987e-3	2.1025
400	0.99536	4.6413e-3	2.0737	0.99549	4.5108e-3	2.0769
625	0.99707	2.9261e-3	2.0674	0.99715	2.8483e-3	2.0603

figure of Figure 2 suggest optimal $\mathcal{O}(h^{p+2})$ convergence rate. Next, we present the global effectivity indices in Table 2. We observe that the error estimators converge to the true errors in the L^2-norm under h-refinement. The errors $|\Theta - 1|$ and their convergence orders shown in Table 2 suggest that the convergence order for $|\Theta - 1|$ is $\mathcal{O}(h^2)$. Again, the observed numerical convergence order is higher than the theoretical order established in Theorem 4.1.

Finally, we solve the same problem but we use the periodic boundary conditions

$$u(0, y) = u(1, y),\ u(x, 0) = u(x, 1), \tag{40f}$$

$$u_x(0, y) = u_x(1, y), \quad u_y(x, 0) = u_y(x, 1),\ (x, y) \in \partial\Omega. \tag{40g}$$

We report the L^2-norm of the errors $\|u_h - \pi u\|$ and $\|e_u - E_u\|$ in Figure 3. We can observe that $\|u_h - \pi u\| = \mathcal{O}(h^{p+2})$ and $\|e_u - E_u\| = \mathcal{O}(h^{p+2})$. Thus, optimal $(p + 2)$-th order can be always achieved. These results are consistent with our theoretical results. Finally, we present the global effectivity indices and the errors $|\Theta - 1|$ in Table 2. These results suggest that the convergence rate for $|\Theta - 1|$ is $\mathcal{O}(h^2)$.

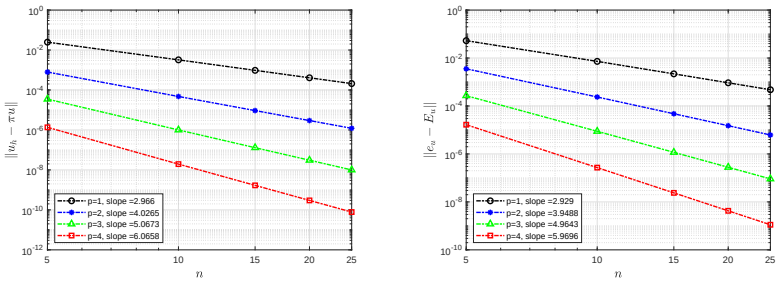

Figure 2: Convergence rates for $\|u_h - \pi u\|$ (left) and $\|e_u - E_u\|$ (right) for the BVP (40a) subject to the mixed boundary conditions (40d-40e) on uniform meshes having $N = 25$, 100, 225, 400, and 625 elements using the spaces $\mathcal{Q}^p$, $p = 1, 2, 3, 4$. The slopes of the fitting lines are shown on the graph.

TABLE 2. Global effectivity indices Θ and the errors $|\Theta - 1|$ for the BVP (40a) subject to the mixed boundary conditions (40d-40e) on uniform meshes having $N = 25$, 100, 225, 400, and 625 elements using $\mathcal{Q}^p$, $p = 1, 2, 3, 4$.

N	$p=1$			$p=2$		
	Θ	$\lvert\Theta-1\rvert$	order	Θ	$\lvert\Theta-1\rvert$	order
25	0.89375	1.0625e-1		0.93624	6.3760e-2	
100	0.97165	2.8349e-2	1.9061	0.98378	1.6220e-2	1.9749
225	0.98723	1.2771e-2	1.9667	0.99276	7.2432e-3	1.9883
400	0.99278	7.2209e-3	1.9820	0.99592	4.0822e-3	1.9933
625	0.99537	4.6336e-3	1.9882	0.99738	2.6152e-3	1.9956
N	$p=3$			$p=4$		
	Θ	$\lvert\Theta-1\rvert$	order	Θ	$\lvert\Theta-1\rvert$	order
25	0.93355	6.6447e-2		0.93388	6.6118e-2	
100	0.98319	1.6809e-2	1.9830	0.98322	1.6781e-2	1.9782
225	0.99251	7.4868e-3	1.9947	0.99252	7.4798e-3	1.9929
400	0.99579	4.2144e-3	1.9975	0.99579	4.2118e-3	1.9964
625	0.99730	2.6981e-3	1.9985	0.99730	2.6970e-3	1.9976

Again, the observed numerical convergence rate is higher than the theoretical order established in Theorem 4.1.

Example 5.2. Here, we apple the LDG method to the following semilinear elliptic problem

$$-u_{xx} - u_{yy} = -u^3 + g(x,y), \quad (x,y) \in [0,1]^2, \tag{41a}$$

where the boundary conditions and the function $g(x,y)$ are extracted from the exact solution

$$u(x,y) = \sin(2\pi x)\sin(2\pi y).$$

We remark that the function $f(\mathbf{x}, u)$ does not satisfy assumptions (1b) and (1c). We consider the purely Dirichlet and mixed boundary conditions. First, we consider (41a) subject to the purely Dirichlet boundary conditions

$$u(x,0) = u(x,1) = u(0,y) = u(1,y) = 0, \quad (x,y) \in \partial\Omega. \tag{41b}$$

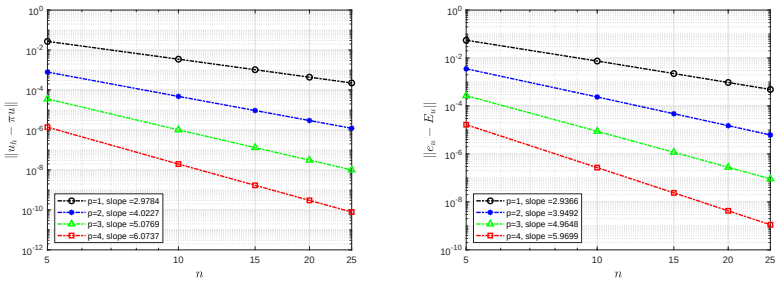

Figure 3: Convergence rates for $\|u_h - \pi u\|$ (left) and $\|e_u - E_u\|$ (right) for the BVP (40a) subject to the periodic boundary conditions (40f-40g) on uniform meshes having $N = 25$, 100, 225, 400, and 625 elements using the spaces $\mathcal{Q}^p,\ p = 1, 2, 3, 4$. The slopes of the fitting lines are shown on the graph.

TABLE 3. Global effectivity indices Θ and the errors $|\Theta - 1|$ for the BVP (40a) subject to the periodic boundary conditions (40f-40g) on uniform meshes having $N = 25$, 100, 225, 400, and 625 elements using $\mathcal{Q}^p,\ p = 1, 2, 3, 4$.

N	$p=1$			$p=2$		
	Θ	$\lvert\Theta-1\rvert$	order	Θ	$\lvert\Theta-1\rvert$	order
25	0.88833	1.1167e-1		0.93635	6.3646e-2	
100	0.97046	2.9543e-2	1.9184	0.98375	1.6248e-2	1.9698
225	0.98673	1.3269e-2	1.9741	0.99275	7.2548e-3	1.9886
400	0.99251	7.4913e-3	1.9872	0.99591	4.0877e-3	1.9941
625	0.99520	4.8026e-3	1.9924	0.99738	2.6182e-3	1.9965
N	$p=3$			$p=4$		
	Θ	$\lvert\Theta-1\rvert$	order	Θ	$\lvert\Theta-1\rvert$	order
25	0.93358	6.6423e-2		0.93380	6.6204e-2	
100	0.98319	1.6806e-2	1.9827	0.98321	1.6793e-2	1.9791
225	0.99251	7.4859e-3	1.9945	0.99252	7.4837e-3	1.9934
400	0.99579	4.2141e-3	1.9973	0.99579	4.2135e-3	1.9968
625	0.99730	2.6980e-3	1.9984	0.99730	2.6978e-3	1.9981

We use the LDG scheme presented in Section 2 to (41a) subject to (41b). The domain $[0, 1]^2$ is partitioned into uniform squares with $h = 1/5$, $1/10$, $1/15$, $1/20$, and $1/25$. We use the finite element spaces with degree $p = 1$, 2, 3, 4. We list the L^2-norm of the errors $\|u_h - \pi u\|$ and $\|e_u - E_u\|$ in Figure 4. We also present the numerical orders of convergence. We observe that the convergence orders meet the theoretical expectation very well. In Table 4, we report the global effectivity index Θ and the error $|\Theta - 1|$ for different N and p. We observe that Θ approaches one under mesh refinement. The numerical results confirm the theoretical analysis. Even though the assumptions (1b) and (1c) do not hold, the same results are observed.

Next, we solve the same problem but we use the mixed Dirichlet-Neumann boundary conditions instead of the Dirichlet boundary conditions. To to more specific, we consider (41a) subject to

(41c) $u(0, y) = u(x, 0) = 0, \quad u_x(1, y) = \cos(y), \quad u_y(x, 1) = \cos(x), \quad (x, y) \in \partial\Omega.$

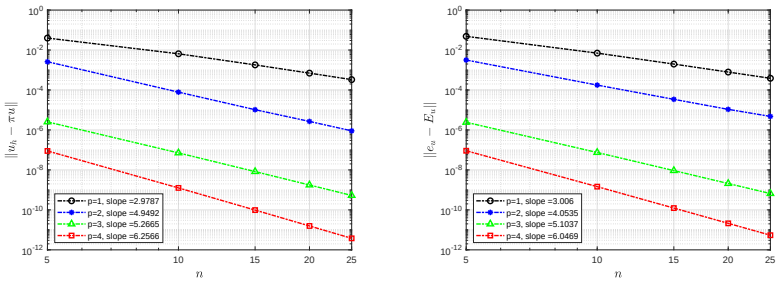

Figure 4: Convergence rates for $\|u_h - \pi u\|$ (left) and $\|e_u - E_u\|$ (right) for the BVP (41a) subject to the Dirichlet boundary conditions (41b) on uniform meshes having $N = 25$, 100, 225, 400, and 625 elements using the spaces $\mathcal{Q}^p$, $p = 1, 2, 3, 4$. The slopes of the fitting lines are shown on the graph.

TABLE 4. Global effectivity indices Θ and the errors $|\Theta - 1|$ for the BVP (41a) subject to the Dirichlet boundary conditions (41b) on uniform meshes having $N = 25$, 100, 225, 400, and 625 elements using $\mathcal{Q}^p$, $p = 1, 2, 3, 4$.

N	$p=1$			$p=2$		
	Θ	$\lvert\Theta-1\rvert$	order	Θ	$\lvert\Theta-1\rvert$	order
25	0.6845	3.1546e-1		1.0271	2.7108e-2	
100	0.8816	1.1839e-1	1.4139	1.0065	6.3536e-3	2.0594
225	0.9509	4.9115e-2	2.1699	1.0029	2.9254e-3	1.9704
400	0.9756	2.4389e-2	2.4334	1.0019	1.8999e-3	1.3504
625	0.9861	1.3903e-2	2.5187	1.0011	1.0528e-3	2.6456
N	$p=3$			$p=4$		
	Θ	$\lvert\Theta-1\rvert$	order	Θ	$\lvert\Theta-1\rvert$	order
25	1.1977	1.9766e-1		1.1439	1.4395e-1	
100	1.0674	6.7353e-2	1.5532	1.0483	4.8271e-2	1.5763
225	1.0301	3.0143e-2	1.9829	1.0215	2.1481e-2	1.9969
400	1.0156	1.5593e-2	2.2912	1.0109	1.0938e-2	2.3461
625	1.0086	8.6353e-3	2.6484	1.0059	5.8926e-3	2.7720

The L^2-norm of the errors $\|u_h - \pi u\|$ and $\|e_u - E_u\|$ are shown in Figure 5 for p= 1, 2, 3, 4. The rates of convergence obtained agree with the theoretical rates of convergence stated in Theorems 26 and 4.1, *i.e.*, our estimates are sharp. Finally, Table 5 displays the global effectivity index Θ and the error $|\Theta - 1|$. We can observe that the global effectivity indices stay close to unity and converge to unity under h-refinement.

Example 5.3. In this example, we consider the following elliptic problem with mixed boundary conditions

$$-u_{xx} - u_{yy} = -\frac{u + 2u^3}{1 + u^2} + g(x, y), \quad (x, y) \in [0, 1]^2, \tag{42a}$$

$$u(x, 0) = 0, \quad u_y(x, 1) = (1 - e)(1 - x)(e^{x^2} - 1), \quad x \in [0, 1], \tag{42b}$$

$$u(0, y) = 0, \quad u_x(1, y) = (1 - e)(1 - y)(e^{y^2} - 1), \quad y \in [0, 1]. \tag{42c}$$

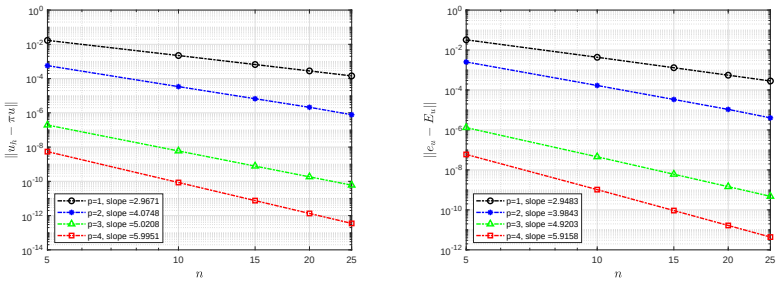

Figure 5: Convergence rates for $\|u_h - \pi u\|$ (left) and $\|e_u - E_u\|$ (right) for the BVP (41a) subject to the mixed boundary conditions (41c) on uniform meshes having $N = 25$, 100, 225, 400, and 625 elements using the spaces $\mathcal{Q}^p$, $p = 1, 2, 3, 4$. The slopes of the fitting lines are shown on the graph.

TABLE 5. Global effectivity indices Θ and the errors $|\Theta - 1|$ for the BVP (41a) subject to the mixed boundary conditions (41c) on uniform meshes having $N = 25$, 100, 225, 400, and 625 elements using $\mathcal{Q}^p$, $p = 1, 2, 3, 4$.

N	$p=1$			$p=2$		
	Θ	$\lvert\Theta-1\rvert$	order	Θ	$\lvert\Theta-1\rvert$	order
25	0.88558	1.1442e-1		0.93537	6.4627e-2	
100	0.96946	3.0540e-2	1.9056	0.98367	1.6331e-2	1.9845
225	0.98626	1.3739e-2	1.9701	0.99272	7.2789e-3	1.9930
400	0.99224	7.7615e-3	1.9850	0.99590	4.0987e-3	1.9963
625	0.99502	4.9776e-3	1.9908	0.99755	2.4512e-3	2.3039
N	$p=3$			$p=4$		
	Θ	$\lvert\Theta-1\rvert$	order	Θ	$\lvert\Theta-1\rvert$	order
25	0.91915	8.0854e-2		0.93050	6.9503e-2	
100	0.96430	3.5695e-2	1.1796	0.96994	3.0057e-2	1.2094
225	0.97753	2.2469e-2	1.1416	0.98130	1.8703e-2	1.1700
400	0.98368	1.6325e-2	1.1104	0.98650	1.3496e-2	1.1342
625	0.98720	1.2801e-2	1.0898	0.98946	1.0536e-2	1.1096

We select the function $g(x, y)$ suitably such that the analytical solution is

$$u(x, y) = (1 - x)(1 - y)(e^{x^2} - 1)(e^{y^2} - 1).$$

We apply the LDG method to this problem. We use a uniform Cartesian mesh with $N = n^2$ squares, where $n = 5$, 10, 15, 20, and 25. The discrete space V_h^p is constructed using piecewise polynomials of uniform degree p, where $p = 1$, 2, 3 and 4. In Figure 6, we list the L^2-norm of the errors $\|u_h - \pi u\|$ and $\|e_u - E_u\|$ on logarithmic scales. We also show the numerical orders of convergence. We observe that $\|u_h - \pi u\| = \mathcal{O}(h^{p+2})$ and $\|e_u - E_u\| = \mathcal{O}(h^{p+2})$. The results showing in Table 6 indicate that the global effectivity index $\Theta \to 1$ under mesh refinement. Once again, the computed order of convergence matches with the theoretical order of convergence derived in Theorems 26 and 4.1.

Example 5.4 (Nonsmooth solutions)**.** In our error analysis, the solution u is assumed to be in $H^{p+2}(\Omega)$ when using piecewise polynomials of degree p. In this example, we consider a problem that does not conform to the theory presented

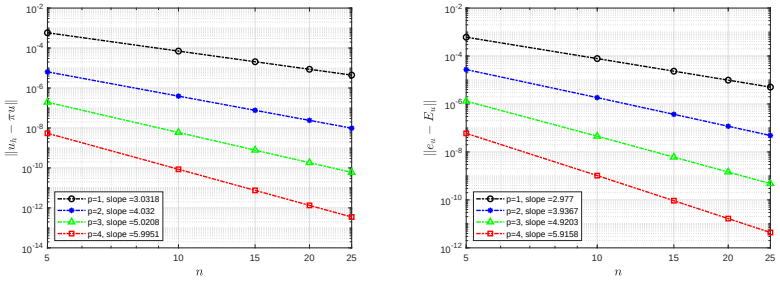

Figure 6: Convergence rates for $\|u_h - \pi u\|$ (left) and $\|e_u - E_u\|$ (right) for the BVP (42a) subject to the mixed boundary conditions (42) on uniform meshes having $N =$ 25, 100, 225, 400, and 625 elements using the spaces $\mathcal{Q}^p$, $p = 1, 2, 3, 4$. The slopes of the fitting lines are shown on the graph.

TABLE 6. Global effectivity indices Θ and the errors $|\Theta - 1|$ for the BVP (42a) subject to the mixed boundary conditions (42) on uniform meshes with $N = 25$, 100, 225, 400, and 625 using $\mathcal{Q}^p$, $p = 1, 2, 3, 4$.

N	$p=1$			$p=2$		
	Θ	$\lvert\Theta-1\rvert$	order	Θ	$\lvert\Theta-1\rvert$	order
25	0.85472	1.4528e-1		0.91184	8.8164e-2	
100	0.93804	6.1958e-2	1.2295	0.96032	3.9684e-2	1.1516
225	0.96058	3.9417e-2	1.1154	0.97477	2.5233e-2	1.1167
400	0.97109	2.8909e-2	1.0777	0.98156	1.8439e-2	1.0904
625	0.97717	2.2826e-2	1.0587	0.98549	1.4512e-2	1.0733
N	$p=3$			$p=4$		
	Θ	$\lvert\Theta-1\rvert$	order	Θ	$\lvert\Theta-1\rvert$	order
25	0.91915	8.0854e-2		0.93050	6.9503e-2	
100	0.96430	3.5695e-2	1.1796	0.96994	3.0057e-2	1.2094
225	0.97753	2.2469e-2	1.1416	0.98130	1.8703e-2	1.1700
400	0.98368	1.6325e-2	1.1104	0.98650	1.3496e-2	1.1342
625	0.98720	1.2801e-2	1.0898	0.98946	1.0536e-2	1.1096

above, with an exact solution that is less regular than $u \in H^{p+2}(\Omega)$. To be more precise, we consider the following boundary-value problem

$$-u_{xx} - u_{yy} = e^{-u} + g(x,y), \quad (x,y) \in [0,1]^2, \tag{43a}$$

$$u(x,0) = \phi_1(x), \quad u_y(x,1) = \phi_2(x), \quad x \in [0,1], \tag{43b}$$

$$u(0,y) = \phi_3(y), \quad u_x(1,y) = \phi_4(y), \quad y \in [0,1]. \tag{43c}$$

We select the functions $g(x,y)$ and ϕ_k, $k = 1, 2, 3, 4$ such that the exact solution is

$$u(x,y) = (\sin(2\pi x) + x^{7/2})(\sin(2\pi y) + y^{7/2}),$$

which is nonsmooth. We remark that $u \in H^3(\Omega)$ but $u \notin H^4(\Omega)$. We apply the LDG scheme using uniform meshes having $N = 100$, 144, 196, 256, 324, and 400 elements and using the spaces $\mathcal{Q}^p$, $p = 2, 3, 4, 5$. Figure 7 presents convergence results for $\|u_h - \pi u\|$ (left) and $\|e_u - E_u\|$ (right). These results indicate that the same rates of convergence as in the smooth solution case are achieved. Table 7 summarizes the global effectivity indices Θ, the errors $|\Theta - 1|$ and their convergence

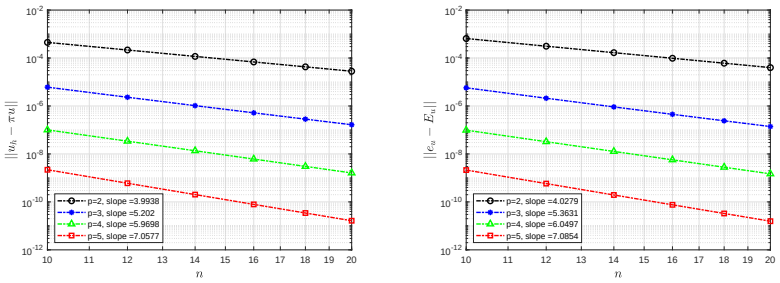

Figure 7: Convergence rates for $\|u_h - \pi u\|$ (left) and $\|e_u - E_u\|$ (right) for the BVP (43) on uniform meshes having $N = 100$, 144, 196, 256, 324, and 400 elements using the spaces $\mathcal{Q}^p$, $p = 2, 3, 4, 5$. The slopes of the fitting lines are shown on the graph.

rates. While our analysis does not cover this case, we observe that our results are in accordance with the prediction of the theoretical analysis for smooth solutions. We leave the analysis of this case (nonsmooth solutions) for future work.

TABLE 7. Global effectivity indices Θ and the errors $|\Theta - 1|$ for the BVP (43) on uniform meshes with $N = 100$, 144, 196, 256, 324, and 400 using $\mathcal{Q}^p$, $p = 2, 3, 4, 5$.

N	$p=2$			$p=3$		
	Θ	$\lvert\Theta-1\rvert$	order	Θ	$\lvert\Theta-1\rvert$	order
100	1.0237	2.3743e-2		1.0219	2.1880e-2	
144	1.0162	1.6249e-2	2.0802	1.0153	1.5319e-2	1.9552
196	1.0118	1.1833e-2	2.0573	1.0113	1.1303e-2	1.9723
256	1.0090	9.0071e-3	2.0436	1.0087	8.6769e-3	1.9801
324	1.0071	7.0881e-3	2.0342	1.0069	6.8677e-3	1.9853
400	1.0057	5.7247e-3	2.0276	1.0056	5.5695e-3	1.9886
N	$p=4$			$p=5$		
	Θ	$\lvert\Theta-1\rvert$	order	Θ	$\lvert\Theta-1\rvert$	order
100	1.0057	5.7018e-3		1.0064	6.4131e-3	
144	1.0040	3.9530e-3	2.0091	1.0045	4.4766e-3	1.9717
196	1.0029	2.9027e-3	2.0035	1.0033	3.2978e-3	1.9825
256	1.0022	2.2218e-3	2.0020	1.0025	2.5291e-3	1.9875
324	1.0018	1.7552e-3	2.0014	1.0020	2.0006e-3	1.9902
400	1.0014	1.4216e-3	2.0007	1.0016	1.6218e-3	1.9923

Example 5.5 (Anisotropic tensor diffusion problem)**.** Consider the following two-dimensional steady state anisotropic tensor diffusion problem

$$-\nabla \cdot (\mathbb{D}\nabla u) = e^{-u} + g(x,y), \quad (x,y) \in [0,1]^2, \tag{44a}$$

$$u(x,0) = \phi_1(x), \quad u_y(x,1) = \phi_2(x), \quad x \in [0,1], \tag{44b}$$

$$u(0,y) = \phi_3(y), \quad u_x(1,y) = \phi_4(y), \quad y \in [0,1], \tag{44c}$$

where the diffusion coefficient tensor is given by

$$\mathbb{D} = \begin{pmatrix} b_1 & -b_2 \\ b_2 & b_1 \end{pmatrix} \begin{pmatrix} d_1 & 0 \\ 0 & d_2 \end{pmatrix} \begin{pmatrix} b_1 & b_2 \\ -b_2 & b_1 \end{pmatrix}.$$

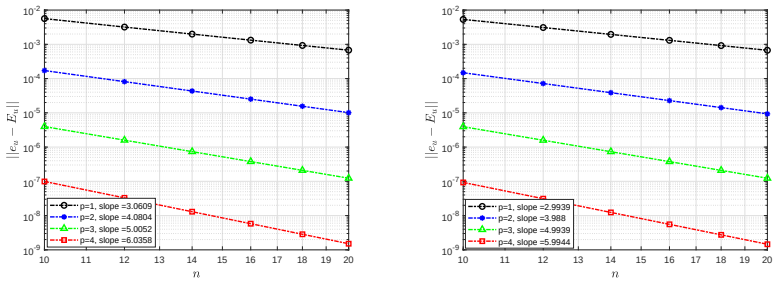

Figure 8: Convergence rates of $\|e_u - E_u\|$ for $d_1 = 1$ (left) and $\|e_u - E_u\|$ for $d_1 = 1000$ (right) for the BVP (44) on uniform meshes having $N = 100$, 144, 196, 256, 324, and 400 elements using the spaces $\mathcal{Q}^p$, $p = 1, 2, 3, 4$. The slopes of the fitting lines are shown on the graph.

The direction of the anisotropy is given by a unit vector $\mathbf{b} = (b_1, b_2)^t$. Here d_1 and d_2 represent the parallel and the perpendicular diffusion coefficients. We take $b_1 = 0$, $b_2 = 1$, $d_2 = 1$, and different values of d_1. We choose the functions $g(x, y)$ and ϕ_k, $k = 1, 2, 3, 4$ such that the exact solution is

$$u(x, y) = \sin(\pi x) \sin(\pi y).$$

Figure 8 shows the convergence rates of $\|e_u - E_u\|$ for an isotropic case $d_1 = 1$ (left) and $\|e_u - E_u\|$ for an anisotropic case $d_1 = 1000$ (right) using polynomial degrees $p = 1$, 2, 3, 4 by using the uniform rectangular meshes. These results show that with anisotropy $d_1 = 1$ and $d_1 = 1000$, the scheme can still produce the optimal rate of convergence for $\|e_u - E_u\|$, which is at the order $\mathcal{O}(h^{p+2})$. As expected, increasing the values of d_1 also increases the L^2-error. However, for low order schemes ($p = 1$ and 2) we do not observe the correct convergence rates when d_1 is a very large number. When the mesh is fine enough, the use of high degree p is able to produce satisfactory numerical solutions with small errors. Also, our numerical experiments show the desired numerical results when we increase the degree of the polynomial p. For the anisotropic case (d_1 is large), we conclude that when we increase the polynomial degree, we recover the expected convergence behavior. We would like to mention that anisotropic meshes are known to be well-suited for problems which exhibit anisotropic solution features in order to provide optimal numerical approximation. We refer to [42] and the references cited therein for more details.

Example 5.6 (Application: Adaptive mesh refinement (AMR) algorithm)**.** Adaptive mesh refinement (AMR) methods based on *a posteriori* error estimates have become a common procedure for obtaining more accurate numerical solutions. AMR methods based on *a posteriori* error estimates have become established procedures for computing efficient and accurate approximations to the solution of differential equations. The key idea of AMR based on *a posteriori* error estimation is to refine those elements which give a large contribution to the estimated error. The typical AMR algorithm is essentially a simple four-step procedure

$$\text{SOLVE} \quad \rightarrow \quad \text{ESTIMATE} \quad \rightarrow \quad \text{MARK} \quad \rightarrow \quad \text{REFINE}.$$

The local *a posteriori* error estimators of section 4 can be used to mark elements for refinement. Next, we present a simple LDG adaptive algorithm based on the local *a posteriori* error estimators proposed in the previous section. It is based on the following steps:

(1) Select a tolerance Tol and a maximum bound on the number of interval N_{max}. Put $\|E_u\| = 1$.
(2) Construct an initial Cartesian grid $\mathcal{T}_h$ consisting of $N = n^2$ square elements $K = [x_{i-1}, x_i] \times [y_{j-1}, y_j] = I_i \times J_j,\ i = 1, 2, \ldots, n,\ j = 1, 2, \ldots, n$, where $I_i = [x_{i-1}, x_i]$, $J_j = [y_{j-1}, y_j]$. For simplicity, we can start with a uniform mesh having $N = 4^2$ square elements.
(3) While $N \leq N_{max}$ and $\|E_u\| \geq Tol$ do the following steps
   (a) Solve the LDG scheme to obtain the LDG solutions u_h and $\mathbf{q}_h$ as described in Section 2.
   (b) For each element $K \in \mathcal{T}_h$, we compute the local error estimators $\|E_u\|_{0,K}$ and the global error estimator $\|E_u\| = \left(\sum_{K \in \mathcal{T}_h} \|E_u\|_{0,K}^2 \right)^{\frac{1}{2}}$.
   (c) For all elements $K \in \mathcal{T}_h$
      (i) Choose a parameter $0 \leq \lambda \leq 1$. If $\|E_u\|_{0,K} \leq \lambda \max_{K \in \mathcal{T}_h} \|E_u\|_{0,K}$ then stop and accept the LDG solutions u_h and $\mathbf{q}_h$ on the element K.
      (ii) Otherwise, reject the LDG solutions on K and divide the element K into 4 square elements by connecting the midpoints of the left and right edges and then the bottom and top edges of the square element K. The advantage of applying the LDG method to elliptic problems relies on the ease with which it handles hanging nodes.
(4) endwhile

Remark 5.1. *There are many possibilities for selecting the elements to be refined given the local error indicator $\|E_u\|_{0,K}$. For example a reasonable approach is to refine the elements satisfying the local error indicator $\|E_u\|_{0,K} > Tol$ and accept the LDG solution u_h on the element I_i if $\|E_u\|_{0,K} \leq Tol$, where Tol is a given tolerance. Also, there are other stopping criteria that may be used to stop the adaptive algorithm. In the above algorithm, we used the most popular fixed-rate strategy which consists of refining the element K if $\|E_u\|_{0,K} > \lambda \max_{K \in \mathcal{T}_h} \|E_u\|_{0,K}$, where $0 \leq \lambda \leq 1$ is a parameter provided by the user. Note that the choice $\lambda = 0$ gives uniform refinement, while $\lambda = 1$ gives no refinement. In practice, the recommended value is $\lambda = 0.5$ which is a natural choice.*

To test our adaptive refinement algorithm, we consider the following convection-diffusion model problem

$$\begin{cases} -\epsilon(u_{xx} + u_{yy}) + u_x + u_y = f(x, y), \quad (x, y) \in [0, 1]^2, \\ u(x, 0) = u(0, y) = u(x, 1) = u(1, y) = 0, \end{cases} \tag{45}$$

where f is chosen in such a way that the exact solution is given by

$$u(x, y) = \left(\frac{e^{\frac{x-1}{\epsilon}} - 1}{e^{-\frac{1}{\epsilon}} - 1} + x - 1 \right) \left(\frac{e^{\frac{y-1}{\epsilon}} - 1}{e^{-\frac{1}{\epsilon}} - 1} + y - 1 \right).$$

We remark that the analytical solution is smooth function, but has boundary layers at $x = 1$ and $y = 1$; see Figure 9 using $\epsilon = 10^{-2}$ (left) and $\epsilon = 10^{-4}$ (right).

To test our AMR algorithm, we take $p = 1,\ 2$ and choose $\epsilon = 10^{-2}$ and $\epsilon = 10^{-4}$. We successively apply adaptive mesh refinement based described above starting with the initial mesh having $N = 16$ elements. In Figures 10 and 11, we show the adaptive meshes using the same tolerance $Tol = 10^{-3}$ for $p = 1, 2$ and $\epsilon =$

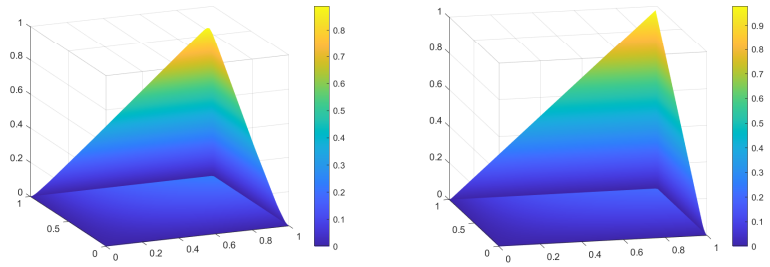

Figure 9: The exact solution os the problem 45 with $\epsilon = 10^{-2}$ (left) and $\epsilon = 10^{-4}$ (right).

10^{-2}, 10^{-4}. We observe strong mesh refinement near the lines $y = 1$ and $x = 1$, indicating that the estimator correctly captures boundary layers. The adaptive code refines elements near the steep gradients. As predicted, we see that the local error estimator is able to refine near the boundary layers.

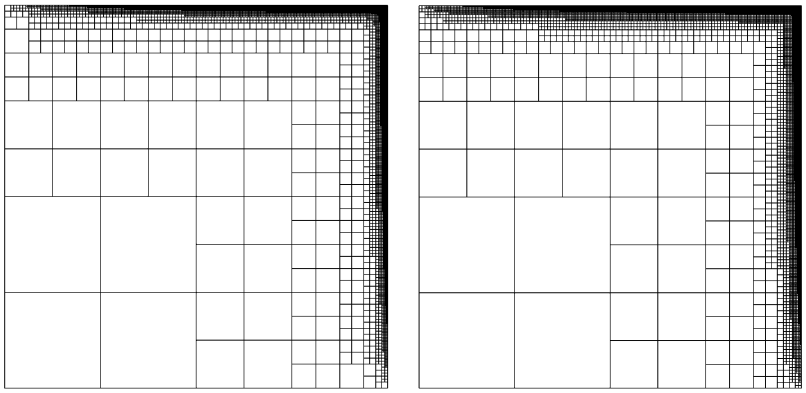

Figure 10: Adaptively refined meshes for Example 5.6 using $p = 1$ with $\epsilon = 10^{-2}$ (left) and $\epsilon = 10^{-4}$ (right).

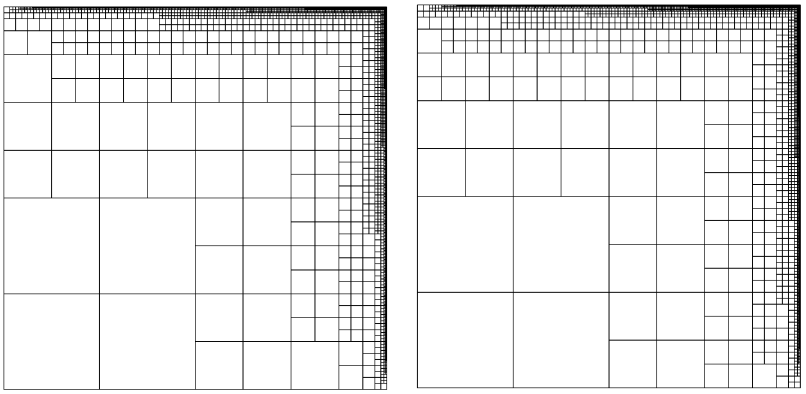

Figure 11: Adaptively refined meshes for Example 5.6 using $p = 2$ with $\epsilon = 10^{-2}$ (left) and $\epsilon = 10^{-4}$ (right).

6. Concluding remarks

In this paper, we designed and studied an implicit residual-based *a posteriori* error estimates for the local discontinuous Galerkin (LDG) method applied to two-dimensional semilinear elliptic problems on a rectangular region. We used our recent optimal superconvergence results [25] to prove that the leading part of the discretization error for the LDG solution is spanned by two $(p+1)$-degree right Radau polynomials in the x- and y- directions, when tensor product polynomials of degree at most p are employed. We used this new result to construct asymptotically exact *a posteriori* error estimator by solving a simple problem on each rectangular element. We further proved that, for smooth solutions, these *a posteriori* error estimators converge to the true errors in the L^2-norm under mesh refinement. The order of convergence is proved to be $p+2$. Finally, we proved that the *a posteriori* error estimator is asymptotically exact. Our numerical experiments demonstrate that the results in this paper hold true for the nonlinear problem (1) with a general function $f(\mathbf{x}, u)$, indicating that the restriction on f is artificial. The generalization of our proofs to nonlinear equations with general function f involves several technical difficulties and will be investigated in the future. We expect that a new technique will be needed to obtain similar superconvergence. In future work, we will also study the superconvergence and error estimation of LDG methods for nonlinear elliptic problems in multidimensional cases on unstructured triangular meshes. We will focus on nonlinear elliptic problems whose solutions have interior layers or sharp boundary. We are also planning to develop *a posteriori* error estimators for the LDG method applied to two-dimensional parabolic and hyperbolic problems on triangular and tetrahedral meshes. Finally, we would like to mention that the analysis of the case of nonsmooth solutions is still an open problem.

Declarations

Conflict of interest: The author declares that he has no conflicts of interest.

Ethical statement: The author declares that the material is his original work, which has not been previously published and is not currently being considered elsewhere.

Data Availability Statement: Data sharing not applicable to this article as no datasets were generated or analysed during the current study.

Acknowledgements: The author would like to thank the anonymous reviewers for the valuable comments and suggestions which improved the quality of the paper.

Funding: This research was partially supported by the NASA Nebraska Space Grant (Federal Grant/Award Number 80NSSC20M0112) and by the University Committee on Research and Creative Activity at the University of Nebraska at Omaha.

References

[1] S. Adjerid and M. Baccouch. A superconvergent local discontinuous Galerkin method for elliptic problems. Journal of Scientific Computing, 52:113–152, 2012.

[2] S. Adjerid and N. Chaabane. An improved superconvergence error estimate for the LDG method. Applied Numerical Mathematics, 98:122 – 136, 2015.

[3] M. Ainsworth. in recent advances in adaptive computation, contemp. math. 383, ams. In A synthesis of *a posteriori* error estimation techniques for conforming, nonconforming and discontinuous Galerkin finite element methods, pages 1–14, 2005.

[4] M. Ainsworth. *A Posteriori* error estimation for discontinuous Galerkin finite element approximation. SIAM Journal on Numerical Analysis, 45(4):1777–1798, 2007.
[5] M. Ainsworth. A framework for obtaining guaranteed error bounds for finite element approximations. Journal of Computational and Applied Mathematics, 234(9):2618 – 2632, 2010.
[6] M. Ainsworth, A. Allendes, G. R. Barrenechea, and R. Rankin. On the adaptive selection of the parameter in stabilized finite element approximations. SIAM Journal on Numerical Analysis, 51(3):1585–1609, 2013.
[7] M. Ainsworth and J. T. Oden. *A posteriori* Error Estimation in Finite Element Analysis. John Wiley, New York, 2000.
[8] D. N. Arnold, F. Brezzi, B. Cockburn, and L. D. Marini. Unified analysis of discontinuous Galerkin methods for elliptic problems. SIAM Journal on Numerical Analysis, 39:1749–1779, 2002.
[9] B. D. B. Cockburn. An analysis of the minimal dissipation local discontinuous Galerkin method for convection-diffusion problems. Journal of Scientific Computing, 32:233–262, 2007.
[10] M. Baccouch. A local discontinuous Galerkin method for the second-order wave equation. Computer Methods in Applied Mechanics and Engineering, 209–212:129–143, 2012.
[11] M. Baccouch. Asymptotically exact *a posteriori* LDG error estimates for one-dimensional transient convection-diffusion problems. Applied Mathematics and Computation, 226:455 – 483, 2014.
[12] M. Baccouch. The local discontinuous Galerkin method for the fourth-order Euler-Bernoulli partial differential equation in one space dimension. Part I: Superconvergence error analysis. Journal of Scientific Computing, 59:795–840, 2014.
[13] M. Baccouch. A superconvergent local discontinuous Galerkin method for the second-order wave equation on Cartesian grids. Computers and Mathematics with Applications, 68:1250–1278, 2014.
[14] M. Baccouch. Superconvergence and *a posteriori* error estimates of the DG method for scalar hyperbolic problems on Cartesian grids. Applied Mathematics and Computation, 265:144 – 162, 2015.
[15] M. Baccouch. Analysis of *a posteriori* error estimates of the discontinuous Galerkin method for nonlinear ordinary differential equations. Applied Numerical Mathematics, 106:129 – 153, 2016.
[16] M. Baccouch. *A Posteriori* error analysis of the discontinuous Galerkin method for two-dimensional linear hyperbolic conservation laws on Cartesian grids. Journal of Scientific Computing, 68(3):945–974, 2016.
[17] M. Baccouch. *A posteriori* error estimator based on derivative recovery for the discontinuous Galerkin method for nonlinear hyperbolic conservation laws on Cartesian grids. Numerical Methods for Partial Differential Equations, 33(4):1224–1265, 2017.
[18] M. Baccouch. Optimal energy-conserving local discontinuous Galerkin method for the one-dimensional sine-Gordon equation. International Journal of Computer Mathematics, 94:316–344, 2017.
[19] M. Baccouch. Superconvergence of the local discontinuous Galerkin method for the sine-Gordon equation on Cartesian grids. Applied Numerical Mathematics, 113:124 – 155, 2017.
[20] M. Baccouch. Asymptotically exact *a posteriori* error estimates for the local discontinuous Galerkin method applied to nonlinear convection-diffusion problems. Journal of Scientific Computing, 76(3):1868–1904, 2018.
[21] M. Baccouch. Superconvergence of the semi-discrete local discontinuous Galerkin method for nonlinear KdV-type problems. Discrete and Continuous Dynamical System - B, 22:1–36, 2018.
[22] M. Baccouch. A superconvergent local discontinuous Galerkin method for nonlinear two-point boundary-value problems. Numerical Algorithms, 79(3):697–718, Nov 2018.
[23] M. Baccouch. Optimal error estimates of the local discontinuous Galerkin method for the two-dimensional sine-Gordon equation on Cartesian grids. International Journal of Numerical Analysis and Modeling, 16:436–462, 2019.
[24] M. Baccouch. Analysis of optimal superconvergence of the local discontinuous Galerkin method for nonlinear fourth-order boundary value problems. Numerical Algorithms, 86(3):1615–1650, 2021.
[25] M. Baccouch. Convergence and superconvergence of a local discontinuous Galerkin method for semilinear second-order elliptic problems on Cartesian grids. Communications on Applied Mathematics and Computation, 4:437–476, 2022.

[26] M. Baccouch and S. Adjerid. Discontinuous Galerkin error estimation for hyperbolic problems on unstructured triangular meshes. Computer Methods in Applied Mechanics and Engineering, 200:162–177, 2010.

[27] M. Baccouch and S. Adjerid. *A posteriori* local discontinuous Galerkin error estimation for two-dimensional convection-diffusion problems. Journal of Scientific Computing, 62:399–430, 2014.

[28] W. Bangerth and R. Rannacher. Adaptive Finite Element Methods for Differential Equations. Birkhäuser Verlag, 2003.

[29] R. Bustinza, G. Gatica, and B. Cockburn. An *A Posteriori* error estimate for the local discontinuous Galerkin method applied to linear and nonlinear diffusion problems. Journal of Scientific Computing, 22:147–185, 2005.

[30] P. Castillo. An *A Posteriori* error estimate for the local discontinuous Galerkin method. Journal of Scientific Computing, 22:187–204, 2005.

[31] P. Castillo, B. Cockburn, I. Perugia, and D. Schötzau. An *a priori* error analysis of the local discontinuous Galerkin method for elliptic problems. SIAM Journal on Numerical Analysis, 38:1676–1706, 2000.

[32] P. G. Ciarlet. The finite element method for elliptic problems. SIAM, 2002.

[33] B. Cockburn. Discontinuous Galerkin methods for computational fluid dynamics. Encyclopedia of Computational Mechanics Second Edition, pages 1–63, 2018.

[34] B. Cockburn, G. Kanschat, I. Perugia, and D. Schötzau. Superconvergence of the local discontinuous Galerkin method for elliptic problems on Cartesian grids. SIAM Journal on Numerical Analysis, 39:264–285, 2001.

[35] B. Cockburn and C. W. Shu. The local discontinuous Galerkin method for time-dependent convection-diffusion systems. SIAM Journal on Numerical Analysis, 35:2440–2463, 1998.

[36] B. Dong and C.-W. Shu. Analysis of a local discontinuous Galerkin method for linear time-dependent fourth-order problems. SIAM Journal on Numerical Analysis, 47:3240–3268, 2009.

[37] H. Dret. Nonlinear elliptic partial differential equations : an introduction. Springer, Cham, 2018.

[38] K. Eriksson, D. Estep, P. Hansbo, and C. Johnson. Computational Differential Equations. Cambridge University Press, Cambridge, 1995.

[39] D. Gilbarg. Elliptic partial differential equations of second order. Springer, Berlin, 2001.

[40] T. Gudi, N. Nataraj, and A. Pani. An *hp*-local discontinuous Galerkin method for some quasilinear elliptic boundary value problems of nonmonotone type. Mathematics of Computation, 77:731–756, 2008.

[41] Q. Han. Elliptic partial differential equations. Courant Institute of Mathematical sciences American Mathematical Society, New York, N.Y. Providence, R.I, 2011.

[42] Y. Huang, Y. Su, H. Wei, and N. Yi. Anisotropic mesh generation methods based on ACVT and natural metric for anisotropic elliptic equation. Science China Mathematics, 56(12):2615–2630, 2013.

[43] O. A. Karakashian and F. Pascal. *A Posteriori* error estimates for a discontinuous Galerkin approximation of second-order elliptic problems. SIAM Journal on Numerical Analysis, 41(6):2374–2399, 2003.

[44] X. Meng, C.-W. Shu, and B. Wu. Superconvergence of the local discontinuous Galerkin method for linear fourth-order time-dependent problems in one space dimension. IMA Journal of Numerical Analysis, 32:1294–1328, 2012.

[45] I. Perugia and D. Schötzau. An hp-analysis of the local discontinuous Galerkin method for diffusion problems. Journal of Scientific Computing, 17(1):561–571, 2002.

[46] W. H. Reed and T. R. Hill. Triangular mesh methods for the neutron transport equation. Technical Report LA-UR-73-479, Los Alamos Scientific Laboratory, Los Alamos, 1973.

[47] C.-W. Shu. Discontinuous Galerkin method for time-dependent problems: Survey and recent developments. In X. Feng, O. Karakashian, and Y. Xing, editors, Recent Developments in Discontinuous Galerkin Finite Element Methods for Partial Differential Equations, volume 157 of The IMA Volumes in Mathematics and its Applications, pages 25–62. Springer International Publishing, 2014.

[48] C.-W. Shu. High order WENO and DG methods for time-dependent convection-dominated PDEs: A brief survey of several recent developments. Journal of Computational Physics, 316:598 – 613, 2016.

[49] E. S. Velázquez and P. E. Castillo. An adaptive strategy for the local discontinuous Galerkin method applied to porous media problems. Computer-Aided Civil and Infrastructure Engineering, 23(4):238–252, 2008.

[50] R. Verfürth. A review of *a posteriori* error estimation and adaptive mesh refinement techniques. Advances in numerical mathematics. Wiley-Teubner, 1996.
[51] H. Wang, C.-W. Shu, and Q. Zhang. Stability analysis and error estimates of local discontinuous Galerkin methods with implicit-explicit time-marching for nonlinear convection-diffusion problems. Applied Mathematics and Computation, 272, Part 2:237 – 258, 2016.
[52] Y. Xu and C.-W. Shu. Error estimates of the semi-discrete local discontinuous Galerkin method for nonlinear convection-diffusion and KdV equations. Computer Methods in Applied Mechanics and Engineering, 196:3805–3822, 2007.
[53] Y. Xu and C.-W. Shu. Local discontinuous Galerkin methods for high-order time-dependent partial differential equations. Communications in Computational Physics, 7:1–46, 2010.

Department of Mathematics, University of Nebraska at Omaha, Omaha, NE 68182, USA
E-mail: mbaccouch@unomaha.edu